2004-06

Numerical prediction of the impact of non-uniform leading edge coatings on the aerodynamic performance of compressor airfoils

Elmstrom, Michael E.

Monterey, California. Naval Postgraduate School

https://hdl.handle.net/10945/1158

NAVAL
POSTGRADUATE
SCHOOL

MONTEREY, CALIFORNIA

THESIS

NUMERICAL PREDICTION OF THE IMPACT OF NON-UNIFORM LEADING EDGE COATINGS ON THE AERODYNAMIC PERFORMANCE OF COMPRESSOR AIRFOILS

by

Michael E. Elmstrom

June 2004

Thesis Advisor:	Knox Millsaps
Second Reader:	Garth Hobson

Approved for public release; distribution is unlimited

REPORT DOCUMENTATION PAGE *Form Approved OMB No. 0704-0188*

1. AGENCY USE ONLY *(Leave blank)*

2. REPORT DATE June 2004

3. REPORT TYPE AND DATES COVERED Engineer and Master's Thesis

4. TITLE AND SUBTITLE: Numerical Prediction of the Impact of Non-Uniform Leading Edge Coatings On the Aerodynamic Performance of Compressor Airfoils.

5. FUNDING NUMBERS

6. AUTHOR(S) Michael Elmstrom

7. PERFORMING ORGANIZATION NAME(S) AND ADDRESS(ES)
Naval Postgraduate School
Monterey, CA 93943-5000

8. PERFORMING ORGANIZATION REPORT NUMBER

9. SPONSORING /MONITORING AGENCY NAME(S) AND ADDRESS(ES)
N/A

10. SPONSORING/MONITORING AGENCY REPORT NUMBER

11. SUPPLEMENTARY NOTES The views expressed in this thesis are those of the author and do not reflect the official policy or position of the Department of Defense or the U.S. Government.

12a. DISTRIBUTION / AVAILABILITY STATEMENT
Approved for public release; distribution is unlimited

12b. DISTRIBUTION CODE

13. ABSTRACT (maximum 200 words)

A computational fluid dynamic (CFD) investigation is presented that provides predictions of the aerodynamic impact of uniform and non-uniform coatings applied to the leading edge of a compressor airfoil in a cascade. Using a NACA 65(12)10 airfoil, coating profiles of varying leading edge non-uniformity were added. This non-uniformity is typical of that expected due to fluid being drawn away from the leading edge during the coating process. The CFD code, RVCQ3D, is a steady, quasi-three-dimensional Reynolds Averaged Navier-Stokes (RANS) solver. A k-omega turbulence model was used for the Reynolds' Stress closure. The code predicted that these changes in leading edge shape can lead to alternating pressure gradients in the first few percent of chord that create small separation bubbles and possibly early transition to turbulence. The change in total pressure loss and trailing edge deviation are presented as a function of the coating non-uniformity parameter. Results are presented for six leading edge profiles over a range of incidences and inlet Mach numbers from 0.6 to 0.8. Reynolds number was 600,000 and free-stream turbulence was 6%. A two-dimensional map is provided that shows the allowable degree of coating non-uniformity as a function of incidence and inlet Mach number.

14. SUBJECT TERMS: Compressor Aerodynamics, Leading Edges, Separation Bubbles, Computational Fluid Dynamics (CFD), Coated Airfoils

15. NUMBER OF PAGES 91

16. PRICE CODE

17. SECURITY CLASSIFICATION OF REPORT	**18. SECURITY CLASSIFICATION OF THIS PAGE**	**19. SECURITY CLASSIFICATION OF ABSTRACT**	**20. LIMITATION OF ABSTRACT**
Unclassified	Unclassified	Unclassified	UL

NSN 7540-01-280-5500 Standard Form 298 (Rev. 2-89)
Prescribed by ANSI Std. 239-18

THIS PAGE INTENTIONALLY LEFT BLANK

NUMERICAL PREDICTION OF THE IMPACT OF NON-UNIFORM LEADING EDGE COATINGS ON THE AERODYNAMIC PERFORMANCE OF COMPRESSOR AIRFOILS

Michael E. Elmstrom
Lieutenant Commander, United States Navy
B.M.E., Georgia Institute of Technology, 1990

Submitted in partial fulfillment of the
requirements for the degree of

MECHANICAL ENGINEER

and

MASTER OF SCIENCE IN MECHANICAL ENGINEERING

from the

NAVAL POSTGRADUATE SCHOOL
June 2004

Author: Michael E. Elmstrom

Approved by: Knox T. Millsaps
Thesis Advisor

Garth V. Hobson
Second Reader

Anthony J. Healey
Chairman, Department of Mechanical and Astronautical Engineering

ABSTRACT

A computational fluid dynamic (CFD) investigation is presented that provides predictions of the aerodynamic impact of uniform and non-uniform coatings applied to the leading edge of a compressor airfoil in a cascade. Using a NACA 65(12)10 airfoil, coating profiles of varying leading edge non-uniformity were added. This non-uniformity is typical of that expected due to fluid being drawn away from the leading edge during the coating process. The CFD code, RVCQ3D, is a steady, quasi-three-dimensional Reynolds Averaged Navier-Stokes (RANS) solver. A k-omega turbulence model was used for the Reynolds' Stress closure. The code predicted that these changes in leading edge shape can lead to alternating pressure gradients in the first few percent of chord that create small separation bubbles and possibly early transition to turbulence. The change in total pressure loss and trailing edge deviation are presented as a function of the coating non-uniformity parameter. Results are presented for six leading edge profiles over a range of incidences and inlet Mach numbers from 0.6 to 0.8. Reynolds number was 600,000 and free-stream turbulence was 6%. A two-dimensional map is provided that shows the allowable degree of coating non-uniformity as a function of incidence and inlet Mach number.

THIS PAGE INTENTIONALLY LEFT BLANK

TABLE OF CONTENTS

I. INTRODUCTION 1
  - A. OVERVIEW 1
  - B. LITERATURE REVIEW 6
  - C. OBJECTIVES 10
  - D. ORGANIZATION 11

II. NUMERICAL METHOD 13
  - A. MODEL OVERVIEW 13
  - B. SOLUTION METHOD 14
    - 1. Grid Definition 14
    - 2. Flow Solution Equations and Assumptions 15
    - 3. Initial Conditions and Boundary Conditions 15
    - 4. Flow Parameters 15
    - 5. Solution Stability and Convergence 16
  - C. GRID RESOLUTION STUDY 17
  - D. VALIDATION OF THE MODEL 18
  - E. TRANSITION MODEL STUDY 21
    - 1. High Reynolds Number / Low Turbulence 21
    - 2. Low Reynolds Number / Low Turbulence 22
    - 3. High Reynolds Number / High Turbulence 22
    - 4. Low Reynolds Number / High Turbulence 23
    - 5. Summary of Transition Model Sensitivity Study 24
  - F. COATING SHAPES 25

III. RESULTS AND DISCUSSION 29
  - A. OVERVIEW 29
  - B. EFFECT OF LEADING EDGE NON-UNIFORMITY 30
  - C. EFFECT OF INLET MACH NUMBER 32
  - D. EFFECT OF INCIDENCE 37
    - 1. Subsonic Cases 37
    - 2. Transonic Cases 40
  - E. DISCUSSION 44
  - F. IMPACT OF LOSS ON ENGINE PERFORMANCE 48

IV. CONCLUSIONS 51

APPENDIX A. AIRFOIL DATA 53

APPENDIX B. GRID GENERATION PARAMETERS 55

APPENDIX C. CFD SOLVER (RVCQ3D) PARAMETERS 57

APPENDIX D. AIRFOIL AND COATING CODE (MATLAB) 59

APPENDIX E. DATA SUMMARY TABLES 63

LIST OF REFERENCES 69
INITIAL DISTRIBUTION LIST 73

LIST OF FIGURES

Figure 1. Two-Dimensional Compressor Cascade Geometry. 3
Figure 2. Airfoil leading edge with no coating, uniform coating, and non-uniform coating. 4
Figure 3. Comparison of the suction side velocity distribution for a smooth leading edge at zero incidence versus and that of a poor leading edge or off-incidence flow. 5
Figure 4. Leading Edge separation bubble due to non-uniform leading edge geometry. 5
Figure 5. NACA 65-(12)10 airfoil profile. 14
Figure 6. Typical Density Residual plot. 16
Figure 7. Final 360x61 Grid with close-up of leading edge region. 18
Figure 8. Empirical Cascade Testing Geometry, After Reference [34]. 18
Figure 9. Pressure Coefficient distribution around airfoil surface for Ma = 0.6: A comparison of experimental results with CFD predictions. 19
Figure 10. Pressure Coefficient distribution around airfoil surface for Ma = 0.76: A comparison of experimental results with CFD predictions. 20
Figure 11. Separation / Transition Sensitivity Study: Distribution of Pressure Coefficient (C_p) Skin Friction (C_F) and Turbulent viscosity (μ_T or mu_T) - (High Re/Low Tu) 21
Figure 12. Separation / Transition Sensitivity Study: Distribution of Pressure Coefficient (C_p) Skin Friction (C_F) and Turbulent viscosity (μ_T or mu_T) - (Low Re/Low Tu) 22
Figure 13. Separation / Transition Sensitivity Study: Distribution of Pressure Coefficient (C_p) Skin Friction (C_F) and Turbulent viscosity (μ_T or mu_T) - (High Re/High Tu) 23
Figure 14. Separation / Transition Sensitivity Study: Distribution of Pressure Coefficient (C_p) Skin Friction (C_F) and Turbulent viscosity (μ_T or mu_T) - (Low Re/Low Tu) 24
Figure 15. Numerical simulation of dried coating on a curved substrate using an initially uniform coating thickness. [From Schwartz, unpublished preliminary results] 25
Figure 16. Family of Coating Curves: Coating thickness near leading edge 27
Figure 17. Leading Edge Profiles (scale is % chord). 28
Figure 18. Pressure Coefficient Distribution versus chord for various coating non-uniformities. 45 degree air inlet and Ma = 0.6. 30
Figure 19. Suction surface pressure coefficient—first one-quarter chord. Various coating profiles at 45 degree inlet angle and Ma = 0.6. 31
Figure 20. Total Pressure Losses ($\bar{\varpi}$) and Turning versus non-uniformity parameter (k): For α = 45 and Ma = 0.6. 32
Figure 21. Losses and turning versus non-uniformity for various inlet Mach numbers ...33

Figure 22. Normalized Losses and Turning versus K for various inlet Mach Numbers...34
Figure 23. Suction Side Pressure Coefficient Distribution (Ma = 0.7) and Turbulent Viscosity (μ_T or mu$_T$) to show why losses for k = 0.75 decrease from k = 0.5.....35
Figure 24. Shift in Pressure Coefficient with Mach for k = 1.....36
Figure 25. Separation Bubble that formed near leading edge of suction surface for Ma = 0.8 and coating parameter, k = 1. 37
Figure 26. Separation Bubble on Suction side that reattached after transition to turbulence for Ma = 0.6, Air Angle of 50 degrees and k = 1.....39
Figure 27. Total Pressure Loss and Deviation versus Inlet Air Angle at Ma = 0.6. 40
Figure 28. Suction Side Pressure Coefficient at four increasing inlet angles for uncoated airfoil at Ma = 0.75.....42
Figure 29. Suction Side Pressure Coefficient and Turbulent Viscosity (μ_T or mu$_T$) showing leading edge shock at 49 degree inlet angle and Ma = 0.75.....43
Figure 30. Total Pressure Loss and Deviation versus Inlet Air Angle at Ma = 0.75 44
Figure 31. Map of Leading Edge Separation Regions: Shows cases with boundary layer separation for a given air angle, Mach number and coating parameter (k).....46
Figure 32. Map of Leading Edge Separation Regions with correlation curves accounting for incidence, Mach number and non-uniformity (k).....48
Figure 33. Contour plot of additional %SFC for an applied coating profile (k) and incidence. (Ma = 0.75).....49

LIST OF TABLES

Table 1. Grid Resolution Study Results. 17
Table 2. Summary of transition simulation showing how predicted total pressure losses and turning are sensitive to changes in Reynolds number and free-stream turbulence. 24
Table 3. Summary of Numerical Investigations. 29
Table 4. Mach Number Effect Simulation Runs 33
Table 5. Incidence angle effect simulation runs (Ma = 0.6) 38
Table 6. Incidence angle effect simulation runs (Ma = 0.75) 41
Table 7. NACA 65 (12)10 Airfoil Coordinates. (From: Ref [36]) 53
Table 8. Additional Circular Leading Edge Points. 53
Table 9. Numerical Simulation Results: Mach number effect. 63
Table 10. Numerical Simulation Results: Ma = 0.6, Negative Incidence. 64
Table 11. Numerical Simulation Results: Ma = 0.6, Zero and Positive Incidence. 65
Table 12. Numerical Simulation Results: Ma = 0.75, Negative Incidence. 66
Table 13. Numerical Simulation Results: Ma = 0.75, Zero and Positive Incidence. 67

THIS PAGE INTENTIONALLY LEFT BLANK

LIST OF SYMBOLS

SYMBOL	**DEFINITION**	**Units or Dimensions**
c	chord length	m
$C_P = \dfrac{p - p_1}{\frac{1}{2}\rho V_1^2}$	pressure coefficient	[1]
h	coating thickness	m
i	incidence	degrees or radians
k	coating non-uniformity parameter	[1]
m	meridional coordinate	m
Ma	Mach number	[1]
p	pressure	Pa
r	leading edge radius	m
Re	Reynolds number	[1]
S	spacing	m
s	path length along airfoil surface	m
Tu	Free-stream turbulence intensity	[1]
V	velocity	m/s
$y^+ = \dfrac{yu^*}{\nu}$	Non-dimensional wall distance	[1]
$u^* = \left(\dfrac{\tau_w}{\rho}\right)^{1/2}$	friction velocity	[1]
α	air angle	degrees
δ	deviation	degrees
θ	circumferential coordinate	radians

λ	stagger	degrees
μ (or mu)	viscosity	Ns/m^2
ρ	density	kg/m^3
$\bar{\varpi}$	total pressure loss	[1]

SUBSCRIPT	**DEFINITION**
1	Inlet
2	Exit
T	Total or Stagnation value
uc	Uncoated
c	Coated

ACKNOWLEDGMENTS

I thank Professor Knox Millsaps for his outstanding guidance and encouragement over the course of this investigation. Additionally, the comments and suggestions on the use of computational fluid dynamics provided by Professor Garth Hobson were invaluable. Further, I thank Professor Len Schwartz for his insights and advice on coating flows that made this study possible. I also thank Professor Chandrasekhara for his valuable suggestions on empirical studies and the expectations for altered airfoil leading edge geometries.

Lastly and most importantly, I express my sincere gratitude and love to my wife Cindy for her continuous and generous support over the past two years.

THIS PAGE INTENTIONALLY LEFT BLANK

I. INTRODUCTION

A. OVERVIEW

Gas turbines are a major source of power and propulsion for industrial and military applications. Due to their high power-to-weight ratio and reliability, aircraft-derivative gas turbine engines such as the General Electric LM2500 and Allison 501 now generate the power for propulsion and electricity for all small and mid-sized U. S. Navy ships. Gas turbines contribute nearly 10% of the energy production capacity in the U. S. Additionally, civilian and military fixed and rotary wing aircraft predominantly use gas turbine engines.

Axial compressors are used in the large gas turbine engines and the performance of these compressors is critical to engine efficiency or specific fuel consumption, power output, and starting time. The compressor is needed to increase inlet air pressure—frequently by 20 to 30 times—prior to combustion. Typically, more than half of the power generated by the turbines is needed to operate the compressor. Therefore, a one-percent drop in compressor efficiency causes more than a one percent penalty in machine capacity and efficiency.

Within a compressor, air flows over alternating rows of fixed and rotating blades or airfoils. Losses within the compressor are minimized by proper design of these blades. The compressor blades must be able to turn and diffuse the flow with minimum relative total pressure loss. Optimally, smoothly accelerating flow over the front of each airfoil allows for an attached laminar boundary layer. As the pressure rises over the remainder of the airfoil, the boundary layer typically undergoes transition to turbulence. If flow or geometric conditions lead to flow separation or early transition to turbulence, losses within each stage will increase at the expense of overall compressor efficiency and pressure rise.

An important geometric concern for the development of the boundary layer is proper control of curvature at the blade's leading edge. This is challenging because the leading edge radius is often less than 1% of the chord length. Poor leading edge shape may lead to excessive acceleration and deceleration of flow near the leading edge, which affects the development of the viscous boundary layer. A leading edge velocity spike followed by an adverse pressure gradient may cause the laminar boundary layer to separate. This separated shear layer usually is unstable and typically reattaches as a turbulent boundary layer leading to increased trailing edge momentum thickness, reduced turning, and lower stall margin. All of these effects documented by Abbott [1] and Gostelow [2] tend to reduce the pressure ratio, efficiency and airflow capacity of the axial compressor.

Figure 1 shows two airfoils arranged as in a two-dimensional cascade. The airfoils have a chord length (c) and spacing (S). They are offset from axial at a stagger angle (λ). Flow enters at a relative inlet air angle (α_1) and velocity (V_1) with total pressure (P_{T1}) static pressure (P_1) and density (ρ_1). Incidence (i) is the angle between the incoming air and the forward extended mean camber line. As the flow leaves the back edge of the airfoil, a wake develops due to the reduced velocity in the boundary layers. Because of the wake, averaging methods are typically used to determine exit values of velocity, pressure, and air angle. This average can be a velocity average or energy average, but must be consistently applied. The total pressure loss is found from the difference between inlet and outlet total pressure. Normally, this value is non-dimensionalized by the dynamic head, $\rho_1 V_1^2 / 2$, or for compressible flow, the difference between inlet total and static pressure, $P_{T1} - P_1$. The turning accomplished is the difference between the relative inlet and outlet flow angles, $\alpha_1 - \alpha_2$. Deviation (δ) is related to turning and is the difference between the averaged exit angle and the trailing edge extended mean camber line.

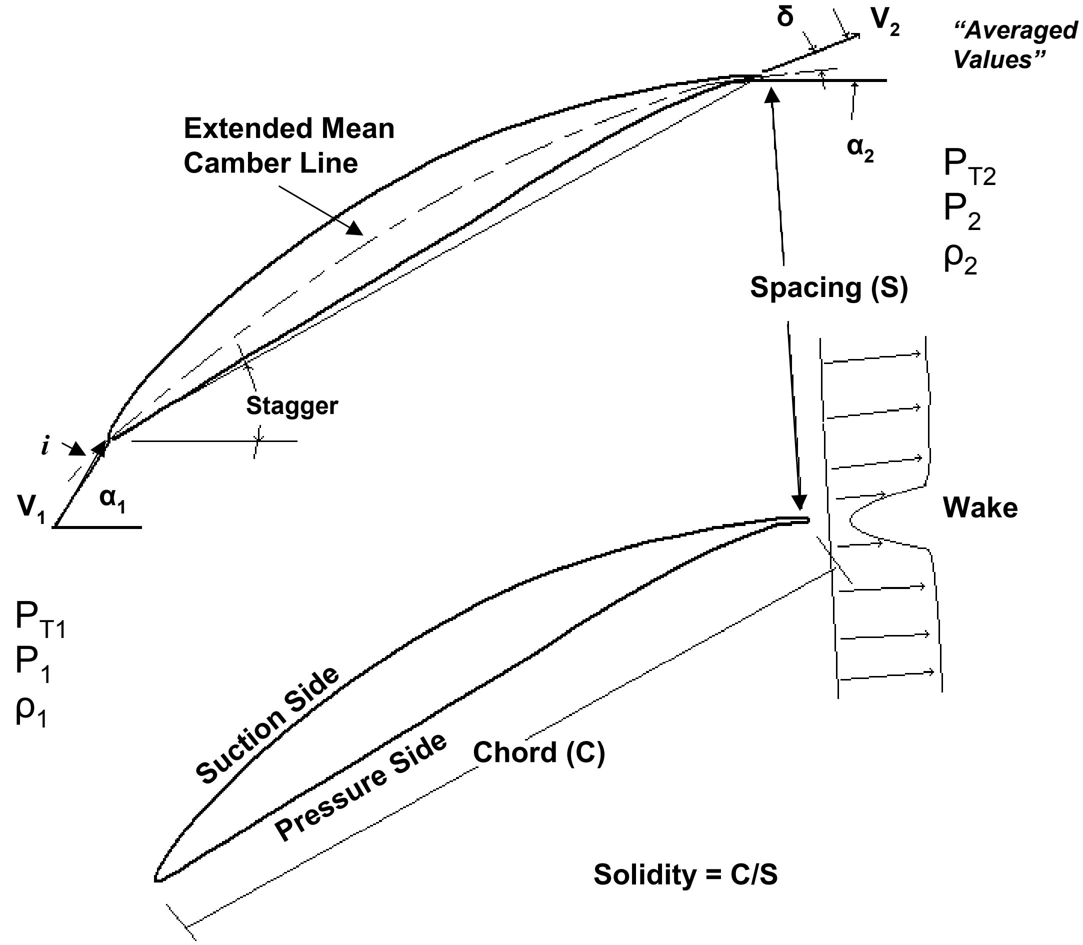

Figure 1. Two-Dimensional Compressor Cascade Geometry.

Unfortunately, in most Naval applications compressor blades experience a hostile environment. Erosion, corrosion, and surface deposition due to ingestion of salt, sand, and oil can alter the airfoil shape and roughen the compressor airfoil. This roughness accelerates the transition to a turbulent boundary layer and can also enhance the frictional shear stress in turbulent regions if the roughness elements penetrate the laminar sublayer [3]. This leads to an increased trailing edge momentum thickness and thus relative total pressure losses and deviation increase. This degrades the performance of the entire compressor, which decreases overall engine efficiency and power.

To combat this degradation, various coatings have been developed to protect the compressor blade surfaces from corrosion and fouling. These coatings, which are typically only about one thousandth on an inch (0.001") thick, are resistant to corrosion and adhesion of foreign particles, while protecting the base metal. Recent testing by Caguiat [4] at Carderock demonstrated how the application of these coatings on compressor airfoils could offset this degradation over time by maintaining a hydrodynamically smooth surface over the entire airfoil.

The leading edge radius for a subsonic inlet compressor airfoil is typically three to seven thousandths of an inch (0.003"-0.007"). If a uniform one-mil (0.001") coating were applied to an airfoil with a nominal 5-mil (0.005") leading edge radius, this would increase the leading edge radius by 20%. This substantial relative thickening of the leading edge, even from a uniform coating could have a negative impact on the airfoil aerodynamics. However, as pointed out by Schwartz [5] in personal discussions the coatings used on these airfoils, which are applied in the liquid state, will have a strong tendency to flow away from the leading edge of the airfoil. This is due to surface tension creating pressure gradients within the drying solvent. These surface tension driven forces are strongest around the sharp leading edge and cause liquid to flow away from the leading edge and hence cause the coating to bunch up behind the corners to form fat edge beads or shoulders near the region where the leading edge blends with the rest of the airfoil. The resulting leading edge coated profile is dependant on airfoil shape, coating application/drying process, and solvent parameters such as viscosity and surface tension. Based on heuristic arguments, it is believed that resulting dried shapes from this non-uniform coating will tend to further degrade the aerodynamic performance from that of a uniform coating. Figure 2 roughly illustrates leading edge profiles of uncoated, uniform coated and non-uniform coated airfoils.

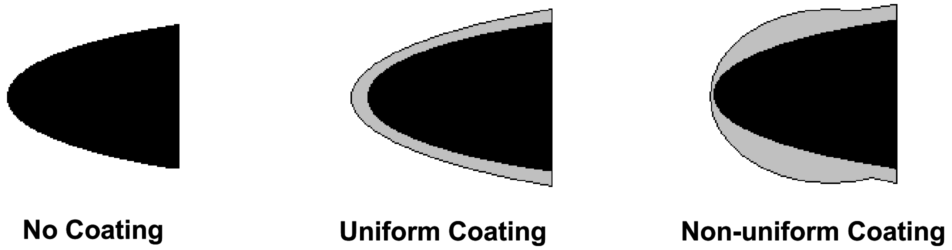

Figure 2. Airfoil leading edge with no coating, uniform coating, and non-uniform coating.

Figure 3 compares a normal velocity distribution with one that may result from off-incidence flow or poor leading edge design. Figure 4 shows the resulting leading edge separation bubble. This leading edge separation bubble indicates a probable adverse impact on aerodynamic performance.

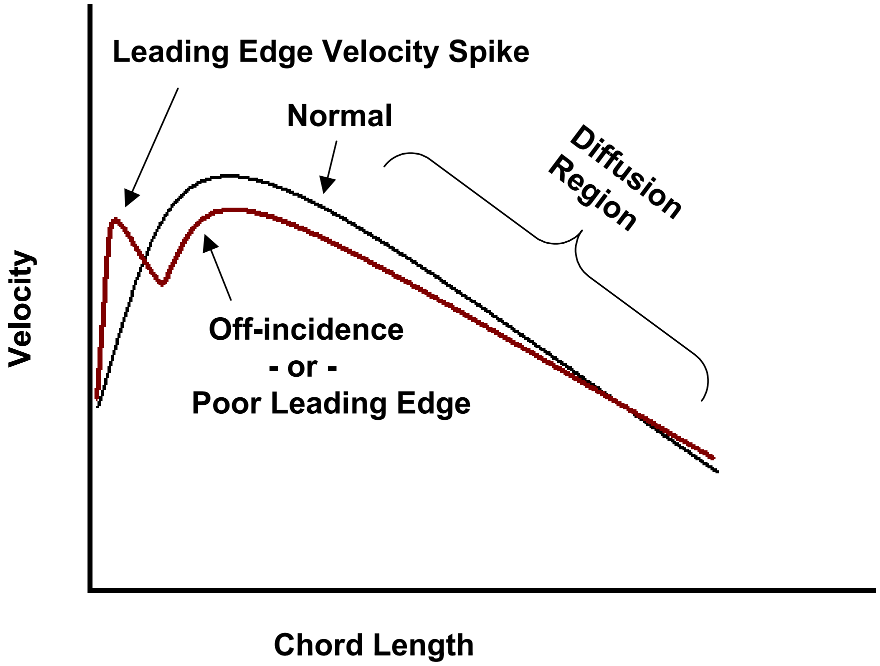

Figure 3. Comparison of the suction side velocity distribution for a smooth leading edge at zero incidence versus and that of a poor leading edge or off-incidence flow.

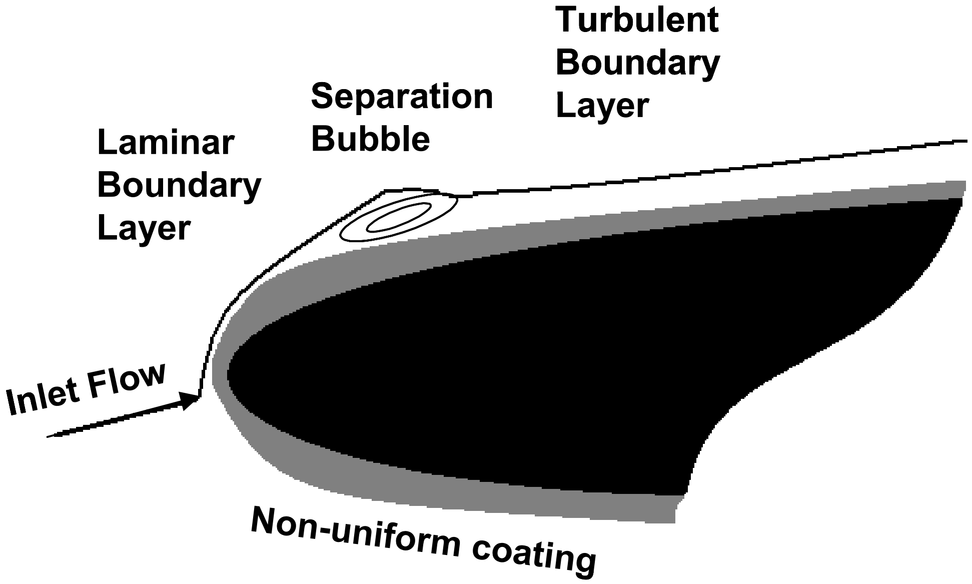

Figure 4. Leading Edge separation bubble due to non-uniform leading edge geometry.

Both the altered shape and increased thickness around the leading edge will have an aerodynamic impact on the development of the boundary layer and thus eventually on overall engine performance. Prediction or measurement of the impact of non-uniform leading edge geometry is important because a 10% relative degradation of total pressure loss and a 5% relative decrease in turning will result in a 1% increase in absolute specific fuel consumption generating a $10 million annual increase in fuel costs for the U. S. Navy's gas turbines alone. An understanding of the impact of poor leading edge geometry will help assess the magnitude of acceptable coating non-uniformity, as well as the importance of initial leading edge manufacturing tolerance and subsequent blade refurbishment.

B. LITERATURE REVIEW

Several studies, such as those by Schwartz and Weidner [6] and Eley and Schwartz [7], have investigated the flow of thin viscous films on curved surfaces. These studies show that surface tension will cause forces within the film that pull coating away from sharp corners. As the film dries, the coating bunches up behind the leading edge forming shoulders or edge beads. Importantly, airfoils with sharp leading edges have a significant ratio of coating thickness to leading edge radius (h/R) so are very susceptible to this phenomenon.

The effect of compressor blade leading edge bluntness has also been investigated. Early efforts by Reid and Urasek [8] in 1973 showed that a blunt leading edge in a supersonic free stream caused a two-to-five point efficiency drop resulting from an increase in the shock losses associated with a detached bow wave system. Roberts [9], in 1984, reported that a blunt leading edge shape due to erosion is a major source of compressor losses. The losses were seen as measurable increases in momentum thickness at the trailing edge due to laminar or turbulent separation caused by velocity spikes near the leading edge. In 1995, Roberts [10] revisited leading edge blunting and reported a 0.7% improvement in thrust specific fuel consumption (TSFC) due to leading edge refurbishment.

More recent studies have investigated the effect of increased leading edge thickness and roughness. In 1995, Suder, et al. [11] reported deterioration of a transonic/supersonic axial compressor rotor due to surface roughness and airfoil thickness variations. They found that a coating caused a thickening of the blade boundary layers. Specifically, coating the first 2% of chord caused almost all of the performance loss from increased thickness. Increased roughness at the leading edge had the largest effect through an interaction between the rotor passage shock wave and the thickened suction surface boundary layer, which increased blockage and reduced diffusion. Similar studies on the affect of ice formation on airfoils by Kwon and Sankar [12], Khalid et al. [13], and, Huebsch and Rothmayer [14] numerically predict aerodynamic losses and dynamic stall due to a non-optimal leading edge shape.

The effect of leading edge shape on separation bubbles has also been demonstrated. In 1991, Tuck [15] found that laminar separation on the leading edge of an airfoil occurs when $i > 0.818\left(\frac{r}{c}\right)^{0.5}$ where i is the incidence angle and $\left(\frac{r}{c}\right)$ is the ratio of leading edge radius to chord. In 1995, Walraevens and Cumpsty [16] studied separation bubbles that form near the leading edge of thin blades of compressors and turbines. They found that non-optimal leading edge shapes drive the formation and size of separation bubbles, which affects development of the boundary layer over the remainder of the airfoil. More recently, Tain [17] investigated the incompressible and compressible flow around the leading edge of a compressor blade. He found that the formation and location of separation bubbles depends on inlet Mach number, incidence and leading edge curvature. Transition length within a separation bubble lessened as incidence, Reynolds number and free stream turbulence increased. In 2003, Huoxing et al [18] also addressed how leading edge shape affects separation bubbles. In general, elliptic leading edge shapes are less prone to separation than circular leading edge shapes.

Computational fluid dynamics (CFD) has been used to predict the losses and turning of a compressor cascade. Many of these codes solve the viscous Navier-Stokes equations using various semi-empirical turbulence models. A major challenge is accurate prediction of separation and transition and has led to several studies over the past decade. In 1991 and again in 1994, Gostelow et al. [19, 20] made correlations of transition length on a flat plate as a function of pressure gradient and free-stream turbulence in order to assist empirical correlations for CFD. Mayle [21] and Walker [22] studied and discussed the laminar-turbulent transition phenomena in gas turbines. They clarified the definition of three transition modes (natural, bypass, and separated flow) and began to examine the influence of pressure gradient and free-stream turbulence on transition initiation and length. Mayle identified roughness and surface curvature as secondary transition initiators.

In 1996, Malkiel and Mayle [23] conducted experiments to help predict separation, transition, and reattachment in laminar separation bubbles. They found the laminar shear layer in a separation bubble is a cross between an attached boundary layer and a free shear layer and so the transition process has elements of each. Also that year, Solomon, Walker, and Gostelow [24] experimentally developed a new method for calculating intermittency in transitional boundary layers with changing pressure gradients by continuously adjusting spot growth parameters in response to changes in the local pressure gradient. These studies showed bypass or separated flow transition are typical in compressor flows.

In contrast, in 1999, Solomon et al. [25] studied transition of an axial compressor blade and found that natural transition modes tend to dominate. Comparisons showed the significance of leading edge potential flow interactions in promoting periodic wake-induced transition. Finally in 2002, Johnson [26] summarized the development of natural transition theory and demonstrated how transition can be predicted from free-stream turbulence intensity and length scale.

With proper semi-empirical calibration of separation and laminar-turbulent transition models, CFD analysis has been used to make qualitative predictions of actual airfoil performance. In 1987, Drela and Giles [27] developed a method to calculate transonic airfoil flows using a viscous-inviscid code. They used an Orr-Sommerfeld transition prediction and could predict separation bubble losses.

Computational methods by Suder, et al. [11] however, generally under-predicted degradations and showed no degradation for a faceted (non-circular) leading edge. In 1998, Sanz and Platzer [28] incorporated a newly developed transition model from Gostelow into an upwind biased Navier-Stokes code to simulate laminar-turbulent transition in the boundary layer. It was capable of predicting laminar separation bubbles on a NACA 0012 airfoil, but they assessed that no reliable method existed to choose the correct transition onset location and spot generation rate.

In 2000, an experimental/computational comparison by Tain and Cumpsty [29] assessed that computational methods were capable of predictive analysis if laminar to turbulent transition is imposed at the start of measured static pressure recovery and if Reynolds stresses are modified for the local, measured Mach number at the edge of the shear layer. Tain [17] used the MISES code by Drela to show how faceted leading edge shapes could be used to minimize or prevent leading edge separation bubbles by minimizing the velocity overshoot in the blend region of the airfoil. More recently, Hobson and Weber [30] compared two CFD schemes in the prediction of leading edge separation bubbles. They found that the quasi-three-dimensional, thin layer Navier-Stokes solver RVCQ3D using explicit time marching and the two-equation k-ω turbulence model by Wilcox [31] performed well in the prediction of total pressure loss, leading edge separation, and wake profile for a controlled diffusion compressor blade in subsonic flow.

Computational fluid dynamics provides solutions to the Navier-Stokes equations. Depending on computational power and Reynolds number of the flow to be simulated, various levels of the actual physics of fluid dynamics can be simulated. The simplest of these Navier-Stokes CFD codes solve the Reynolds Averaged Navier Stokes (RANS) equations using thin layer assumptions and a turbulence model for the Reynolds' stress closure. At a higher level of complexity are large eddy simulations (LES). Finally, direct numerical simulation (DNS) is used to solve the Navier Stokes equations over the entire flow field. Currently, DNS is limited to problems with Reynolds numbers more than two orders of magnitude less than required for compressor aerodynamics.

In summary, it is known that degradation to an airfoil leading edge such as that from blunting, roughening, or ice accretion results in a measurable increase in boundary layer growth. It is also known that flow over a non-uniform surface results in accelerations and decelerations. It has been demonstrated that off-incidence flow leads to possible leading edge separation bubbles. Further, it is known that separated flow typically undergoes transition in a method possibly related to detached shear flows and which is dependent on free stream turbulence and Reynolds number. Once transition occurs these bubbles normally reattach as turbulent boundary layers. It is believed that the momentum thickness of these boundary layers is higher than that of turbulent layers from natural or bypass transition.

It is less well known how accelerations and decelerations of flow over a non-uniform leading edge affect development of the boundary layer. It is not known exactly how these varied leading edge shapes drive possible boundary layer separation. It is not known how these non-uniform leading edge shapes affect the transition to a turbulent boundary layer. Because of this, changes in trailing edge momentum thickness or turbulent separation, which drive total pressure losses and turning are not well known.

It has been demonstrated using computational fluid dynamics involving a viscous boundary layer solution coupled with an inviscid free stream solution that leading edge geometry affects boundary layer separation. These results are limited in that the Navier-Stokes equations are not solved over the entire flow field. Little work has been done using a RANS solver with newer Reynolds' stress turbulence models to study leading edge flow. Further, the effect of leading edge geometric variability on total pressure loss and turning has not been determined. Specifically, an acceptable level of leading edge non-uniformity has not been determined.

C. OBJECTIVES

The objectives of this study are to:

1) Validate and calibrate the CFD code, RVCQ3D, using existing experimental data.

2) Demonstrate that this code's predictions of separation, transition, and total pressure losses are sensitive to inlet conditions such as turbulence and Reynolds number.

3) Numerically determine the changes in total pressure loss and turning of a compressor cascade as a function of the non-uniformity of the leading edge geometry.

4) Set limits of acceptable leading edge coating non-uniformity.

D. ORGANIZATION

Chapter II describes the analytical model including the CFD software and the solution method. It includes a grid resolution study, model validation, and transition sensitivity analysis. Finally, it discusses the development of various leading edge coating profiles.

Chapter III presents and discusses the numerical results obtained for various coating profiles over a range of inlet Mach numbers and incidence angles. A two-dimensional map showing the occurrence of leading edge separation bubbles as a function of incidence, Mach number, and leading edge non-uniformity is also presented.

Chapter IV provides conclusions and recommendations.

THIS PAGE INTENTIONALLY LEFT BLANK

II. NUMERICAL METHOD

A. MODEL OVERVIEW

This study used GRAPE 2-D to generate C-type grids around blade sections. GRAPE (GRids about Airfoils using Poisson's Equation) is a grid generator code created by Reece Sorenson [32, 33] and modified by Rod Chima to allow periodic boundary conditions for turbomachinery applications. The code allowed specification of the inner—or blade surface—boundary points, grid size, and key parameters to control spacing and intersection angles in the streamwise and surface normal directions. From the solution of the Poisson equation, GRAPE outputs the grid points around the blade. The output file, *fort.1*, was viewable using FAST, a flow visualization tool. For further information on the code the reader is referred to the GRAPE 2D User's Manual [34].

The viscous flow solutions were obtained using RVCQ3D (Rotor Viscous Code Quasi-3D) developed by Rod Chima [35, 36]. RVCQ3D solves the viscous, two-dimensional, Navier-Stokes equations using an explicit, four-stage Runge-Kutta scheme that marches in time from an initial guess to a steady-state solution. It is quasi-3d in that it accounts for the three-dimensional effects of rotation, radius change, and stream surface thickness variation.

RVCQ3D includes three turbulence models, the Baldwin-Lomax and Cebeci-Smith algebraic models, and the Wilcox two-equation k-ω turbulence model. This study utilized the low Reynolds number version of the k-ω turbulence model developed by Wilcox [31] due to its ability to model transition effects. The k-ω turbulence model by Wilcox is based on studies of Kolmogorov and includes transport equations for turbulent kinetic energy and turbulent vorticity. This turbulence model can describe the variation of turbulent kinetic energy close to a solid wall boundary and has some capability to predict transition location—visible in the output file as an increase in turbulent viscosity along the airfoil surface.

RVCQ3D provides an output file and two grid solutions viewable with the flow visualization software, FAST. The output file, *rvcq3d.out*, includes a convergence history, energy averaged flow conditions at the inlet and outlet, and final blade surface distributions of pressure, velocity, turbulent viscosity, surface skin friction, and y+ of the first normal grid point. The first grid solution file, *fort.3*, provides flow conditions at each grid point. The second grid solution file, *fort.8*, provides the turbulent values of kinetic energy, vorticity, viscous flux, and effective viscosity throughout the grid. For further information on the code the reader is referred to the RVCQ3D User's Manual [37]. Both RVCQ3D and GRAPE are Fortran programs, which were compiled and executed on a UNIX-based, Silicon Graphics, Octane or Octane-2 workstation.

B. SOLUTION METHOD

1. Grid Definition

The NACA 65-(12)10 airfoil section was selected as a generic, high-subsonic axial-flow compressor blade. Airfoil coordinates were obtained from Felix and Emery [38] and are shown in Appendix A. Leading edge points were fit to a circle that was faired to the surface coordinates. The profile of this airfoil is shown in Figure 5.

Figure 5. NACA 65-(12)10 airfoil profile.

The GRAPE input file, *cdnew.ing*, included these points as well as key parameters to control the grid size and construction. In this study, a cubic spline was used to fit additional points between the between the 59 user specified points. Hermite polynomial clustering controlled the outer boundary spacing to best match the clustering near the blade's leading and trailing edges. In general, the grid size should be refined enough such that solution errors are independent of the grid size. A grid resolution study discussed below was used to determine an optimal grid size. For this study on the effect of leading edge non-uniformities, a tight spacing of points at the leading edge was needed for surface resolution. This was accomplished through the use of the GRAPE parameters NLE—which sets the number of leading edge points—and DSLE—which sets the spacing of the leading edge points. In the blade-to-blade direction, enough points were needed for an accurate viscous solution. For CFD with transitional and turbulent flow, the first several normal grid points should be within the laminar sublayer (y+ < 10). This is controlled by the number of blade-to-blade points and by the parameter DSI, which sets the exponential spacing away the airfoil surface. Additional discussion of specific grid parameters for this study can be found in Appendix B.

2. Flow Solution Equations and Assumptions

A detailed description of Chima's quasi-three-dimensional scheme can be found in Ref [35]. Therefore, the next few sections will emphasize key points from his discussion. The derivation begins with the dimensionless, conservative form of the Navier-Stokes equations in an axi-symmetric coordinate system of two dimensions, m and θ. The meridional coordinate, m, is along the airfoil and is defined by $dm^2 = dz^2 + dr^2$ and the circumferential coordinate, θ, is in the blade-to-blade direction. The final four equations include the continuity equation, two momentum equations, and the energy equation.

The equations assume constant specific heats and a constant Prandtl number. Stokes' hypothesis is assumed valid so that the second coefficient of viscosity is $\lambda = -(2/3)\mu$. Additionally, total or effective viscosity comes from $\mu = \mu_{lam} + \mu_{turb}$. Of note, Chima used the thin-layer assumption in the boundary layer to eliminate the streamwise viscous derivatives thus simplifying the model, while still allowing separated flow determination.

3. Initial Conditions and Boundary Conditions

Because constant initial conditions could cause numerical difficulties, the solver first determines the variable area, one-dimensional analytic solution. This solution is then set as the initial conditions through the grid. The user specifies required inlet and outlet boundary conditions. For subsonic inlet conditions, total pressure, total temperature and whirl, rv_θ are specified. Isentropic relations determine density and energy. At the exit, static pressure is specified. The airfoil surface is adiabatic and for viscous problems the no slip condition exists. Periodic boundary conditions are also applied at +/- one-half pitch to model a turbomachinery cascade. Finally, inlet boundary conditions for free-stream turbulent intensity and viscosity are specified.

4. Flow Parameters

The key flow parameters varied for this study were inlet Mach number, inlet airflow angle, and the static pressure ratio. Chapter III discusses the simulation runs at varying Mach number and incidence. Other parameters that strongly affect separation and transition were the Reynolds number, and the values of free-stream turbulence intensity and length scale. A brief study of the effect of these parameters on transition is discussed in part E of this chapter. A further discussion of the remaining RVCQ3D parameters used is found in Appendix C.

5. Solution Stability and Convergence

As an explicit numerical scheme, stability would normally require a Courant-Friedrichs-Levy number (CFL) of unity or less. This code used a four-stage Runge-Kutta method with residual smoothing allowing a theoretical CFL of up to 5.6. Convergence of residuals was monitored to achieve five orders of magnitude convergence of density such that both pressure distribution and drag calculations were valid. This was generally achieved in 12000 iterations using a CFL of four as shown in Figure 6.

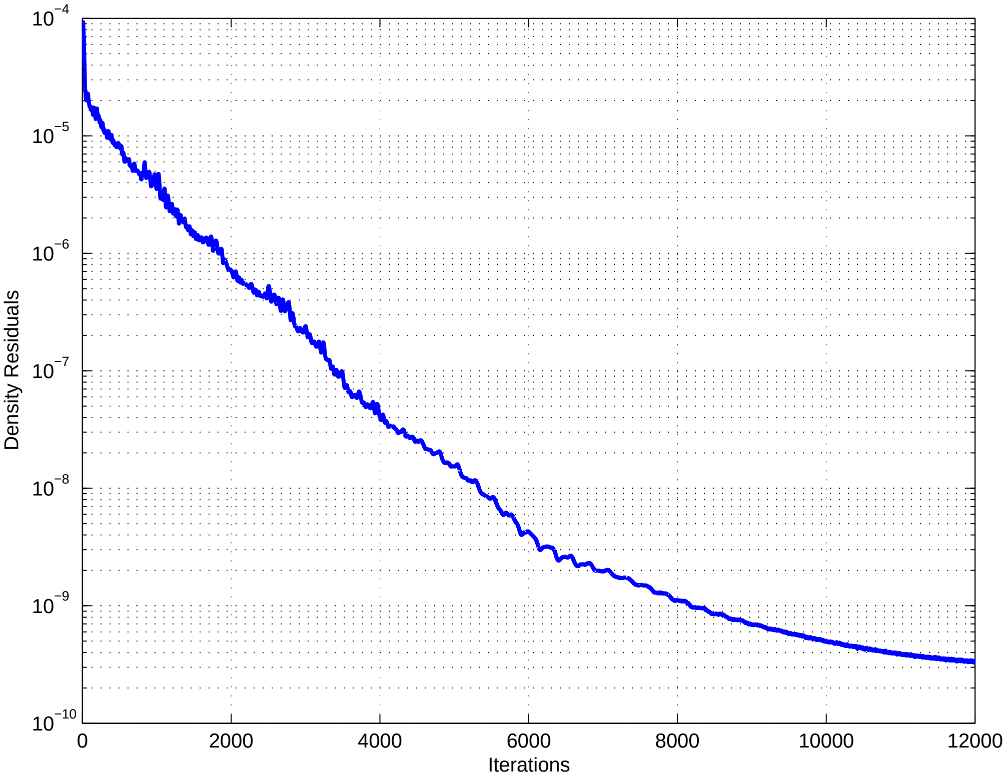

Figure 6. Typical Density Residual plot.

C. GRID RESOLUTION STUDY

One critical parameter when using CFD is the grid size. In general, a larger, more refined grid provides a better solution at the expense of computational time. In order to eliminate errors due to grid refinement, a grid independence study was conducted using two Mach number cases (0.6 and 0.76). The criteria for grid resolution were (1) first y+ less than 2-3 for good loss prediction and (2) grid independence, meaning a larger grid did not significantly change losses and turning. Total pressure loss $\bar{\varpi}$ is defined by

$$\bar{\varpi} = \frac{p_{T1} - p_{T2}}{p_{T1} - p_1} \tag{1}$$

where p_{T1} and p_{T2} are the inlet and exit total pressures and p_1 is the inlet pressure. Turning is defined by

$$Turning = \alpha_1 - \alpha_2 \tag{2}$$

where α_1 and α_2 are the inlet and exit air angles. The Table 1 summarizes the results.

Table 1. Grid Resolution Study Results.

Grid Size (overall)	Grid Size (w/o wake)	Mach #	Total Pressure Loss (%)	Turning (degrees)	1st y+ (min-max)
240x46	160x46	0.60	2.0173	24.7580	0.16-3.07
300x61	200x61	0.60	1.9231	24.6294	0.02-1.33
360x61	200x61	0.60	1.9312	24.6614	0.03-1.33
360x61	240x61	0.60	1.9410	24.4981	0.03-1.33
240x46	160x46	0.76	3.1048	22.9816	0.11-3.14
300x61	200x61	0.76	2.9318	22.8281	0.038-1.35
360x61	200x61	0.76	2.9011	22.8261	0.039-1.35
360x61	240x61	0.76	2.8750	22.8163	0.037-1.35

These runs resulted in the selection of a 360x61 grid with 80 points in the wake for a total of 200 points along the airfoils and 61 points in the blade-to-blade direction. This allows enough points on the airfoil especially in the leading edge region to identify possible separation. Additionally, it maintains high resolution in the wake region, which is important for calculating exit parameters that contribute to losses and turning. Lastly, computational time for the 12,000 iterations is maintained less than one hour on the Silicon Graphics Octane workstations. Figure 7 shows the final grid with a close up around the leading edge.

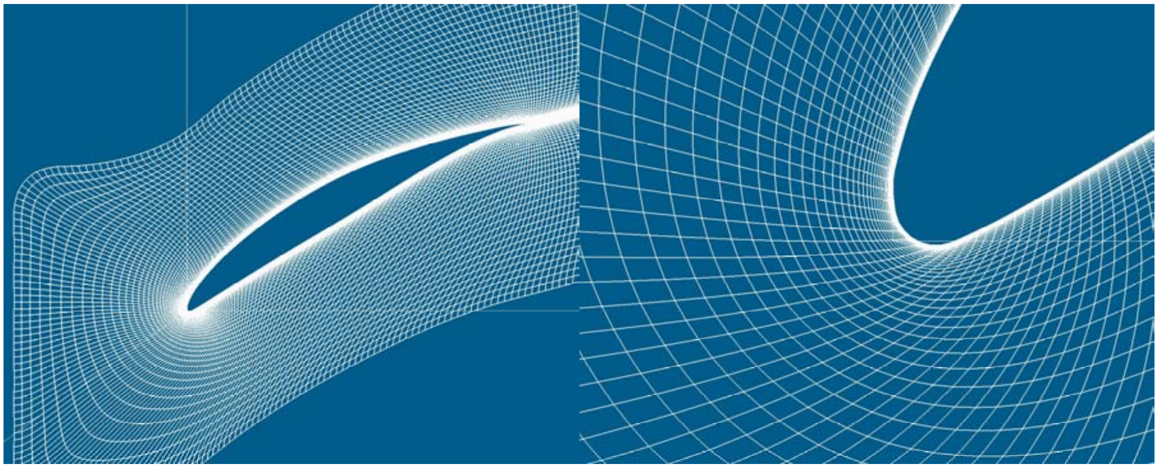

Figure 7. Final 360x61 Grid with close-up of leading edge region.

D. VALIDATION OF THE MODEL

In order to demonstrate the ability of RVCQ3D to match experimental NACA65-(12)10 cascade flow, two test cases were used. The test cases came from subsonic-transonic compressor cascade studies by Briggs [39]. He compared cascade flows with and without porous wall boundary layer suction over a range of inlet Mach numbers from 0.12 to 0.89. This study uses his empirical results from the 0.6 and 0.76 Mach number cases with suction applied so that two-dimensional flow was achieved. Figure 8 shows a diagram of the important geometrical and flow conditions from his experimental work.

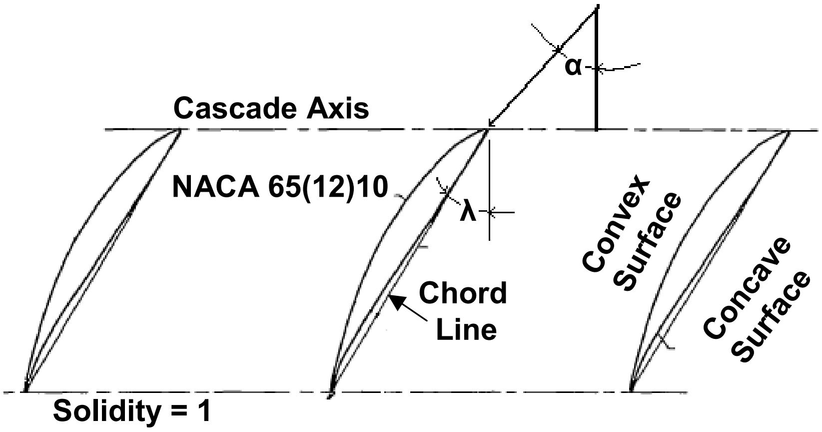

Figure 8. Empirical Cascade Testing Geometry, After Reference [34].

For the empirical testing, the stagger angle (λ) was 28.5 degrees and the inlet airflow angle (α) was 45 degrees. Figures 9 and 10 show the blade surface distribution of the pressure coefficient (C_p) defined by

$$C_P = \frac{p - p_1}{\frac{1}{2} \rho V_1^2} \tag{3}$$

where p is the local static pressure, p_1 is the upstream static pressure, and $\rho V_1 / 2$ is the inlet dynamic head. The numerical simulation runs were made at two different Mach numbers, Ma = 0.6 and Ma = 0.76. Inlet air angle, pressure ratio, turbulence and Reynolds number were varied to match the empirical results. For the final results, Reynolds number was 600,000 and 700,000 respectively with 1% free-stream turbulence intensity for each case.

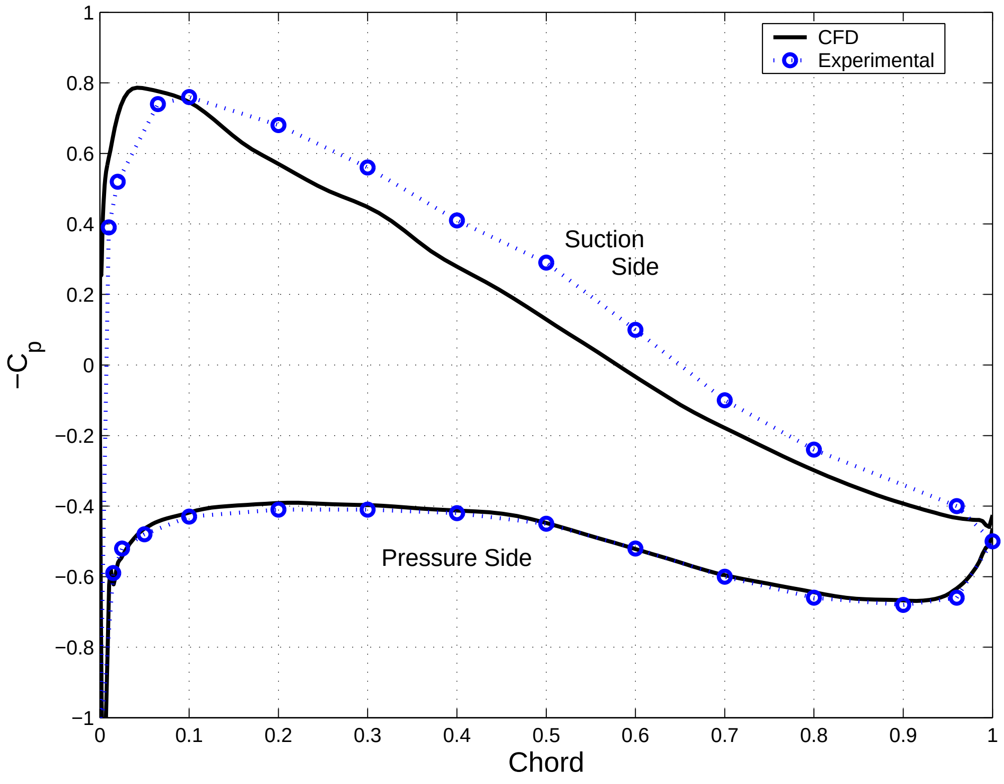

Figure 9. Pressure Coefficient distribution around airfoil surface for Ma = 0.6: A comparison of experimental results with CFD predictions.

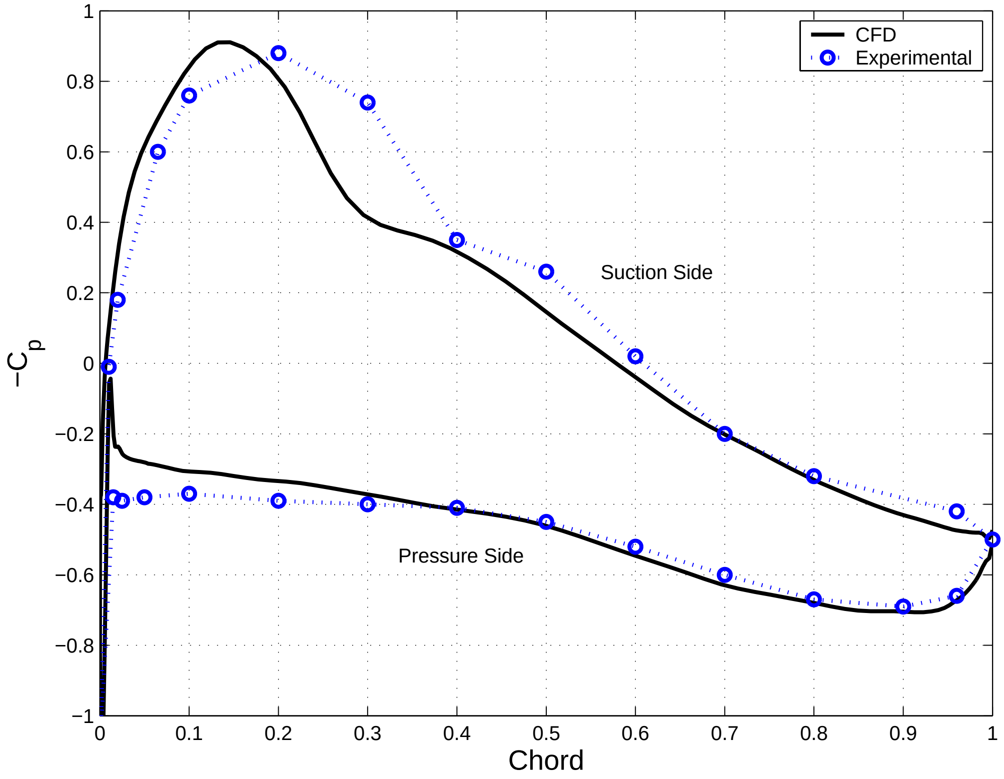

Figure 10. Pressure Coefficient distribution around airfoil surface for Ma = 0.76: A comparison of experimental results with CFD predictions.

The figures of pressure coefficient distribution show that pressure side distributions were closely approximated. On the suction side, some differences are clear. First, for the 0.6 Mach number case, the numerical peak C_p occurs slightly prior to the experimental result. Additionally, the C_p after 10% chord is consistently less than experimental. Next, for the 0.76 Mach number case, the major difference is that the numerically predicted shock occurs prior to the experimentally measured shock. Again, the predicted C_p on the suction side is slightly below the experimentally measured C_p after 20% chord. A slight incidence difference also exists.

Differences may be partially attributed to measurement precision for the 1952 data. Another possibility is differences in the axial velocity density ratio (AVDR). Further, while the numerical prediction may not be exact, RVCQ3D can approximate flow across this airfoil showing criteria such as shocks and flow separation.

E. TRANSITION MODEL STUDY

RVCQ3D with the low Reynolds number k-ω turbulence model has the ability to predict separation bubbles and transition location as a function of free stream turbulence intensity. Several cases using different chord-based Reynolds numbers (400,000 and 800,000) and free stream turbulence levels (1% and 8%) were developed. These were used to see if different locations and methods of transition such as bypass, natural, and separated flow transition could be predicted. The four cases are summarized below.

1. High Reynolds Number / Low Turbulence

A small separation bubble occurs on the suction side at 30% chord resulting in transition to turbulence. Both suction and pressure side boundary layers are laminar until a turbulent boundary layer is needed for additional pressure recovery. Natural transition seems to occur on the pressure side. The lowest losses and highest turning are associated with this region. Figure 11 shows these results.

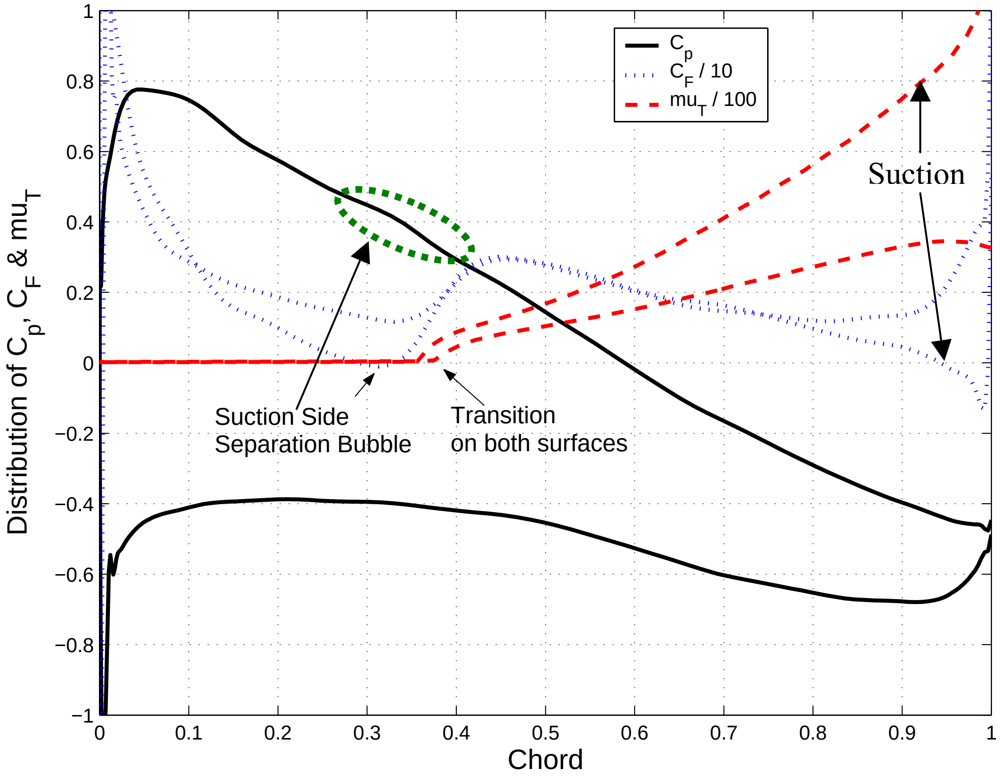

Figure 11. Separation / Transition Sensitivity Study: Distribution of Pressure Coefficient (C_p) Skin Friction (C_F) and Turbulent viscosity (μ_T or mu_T) - (High Re/Low Tu)

2. Low Reynolds Number / Low Turbulence

This low Reynolds flow nearly separates at 22% chord on the suction side. Instead, early transition to turbulence on suction side occurs. Then, significant turbulent separation occurs on the suction side beyond 80% chord. On the pressure side, low Re and low turbulence delay transition until separation occurs at 62% chord. This results in high losses and the lowest turning. Figure 12 shows these results.

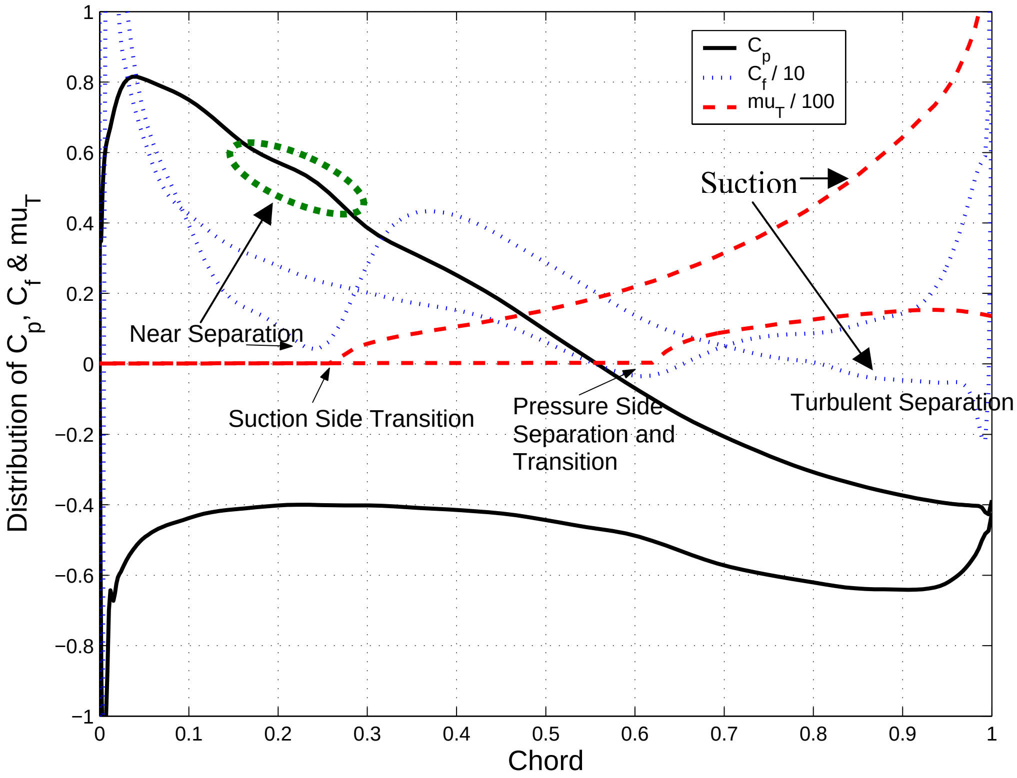

Figure 12. Separation / Transition Sensitivity Study: Distribution of Pressure Coefficient (C_p) Skin Friction (C_F) and Turbulent viscosity (μ_T or mu_T) - (Low Re/Low Tu)

3. High Reynolds Number / High Turbulence

This case has the earliest boundary layer transitions to turbulence on both suction and pressure surfaces. Bypass transition modes appear to dominate. However, since no separation occurs, losses remain low relative to the low Reynolds cases. Figure 13 shows these results.

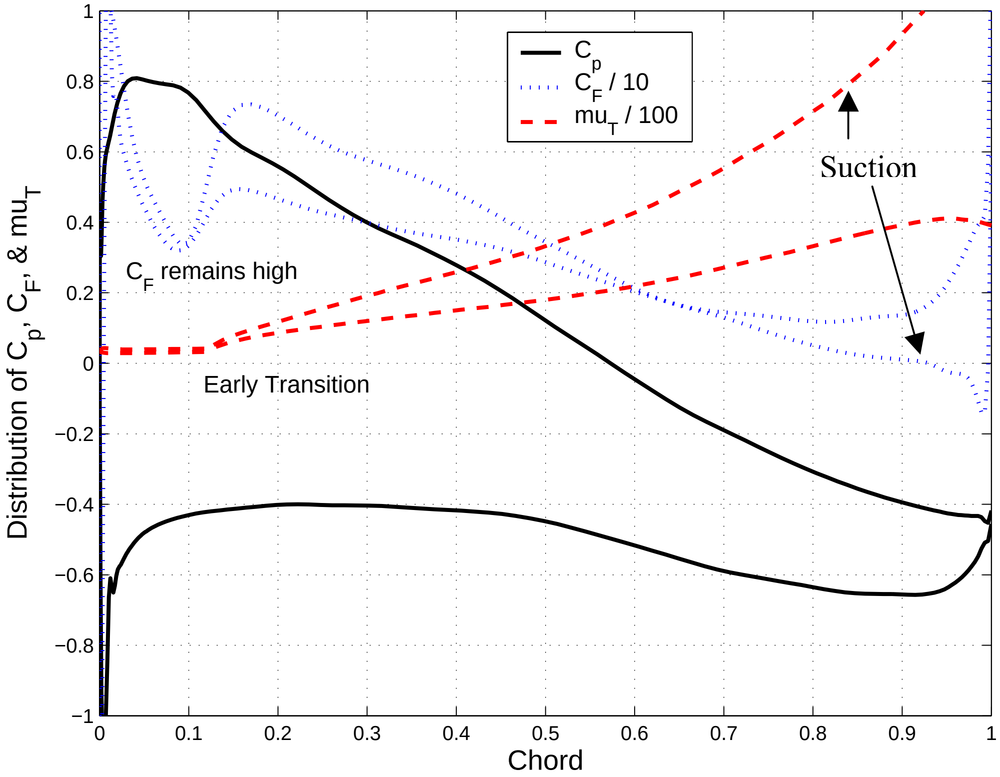

Figure 13. Separation / Transition Sensitivity Study: Distribution of Pressure Coefficient (C_p) Skin Friction (C_F) and Turbulent viscosity (μ_T or mu_T) - (High Re/High Tu)

4. Low Reynolds Number / High Turbulence

Here transition is predicted at about 20% chord on both surfaces. On the suction side, turbulent separation occurs at 80% chord. The result is the highest total pressure loss and nearly the least turning accomplished. Figure 14 shows these results.

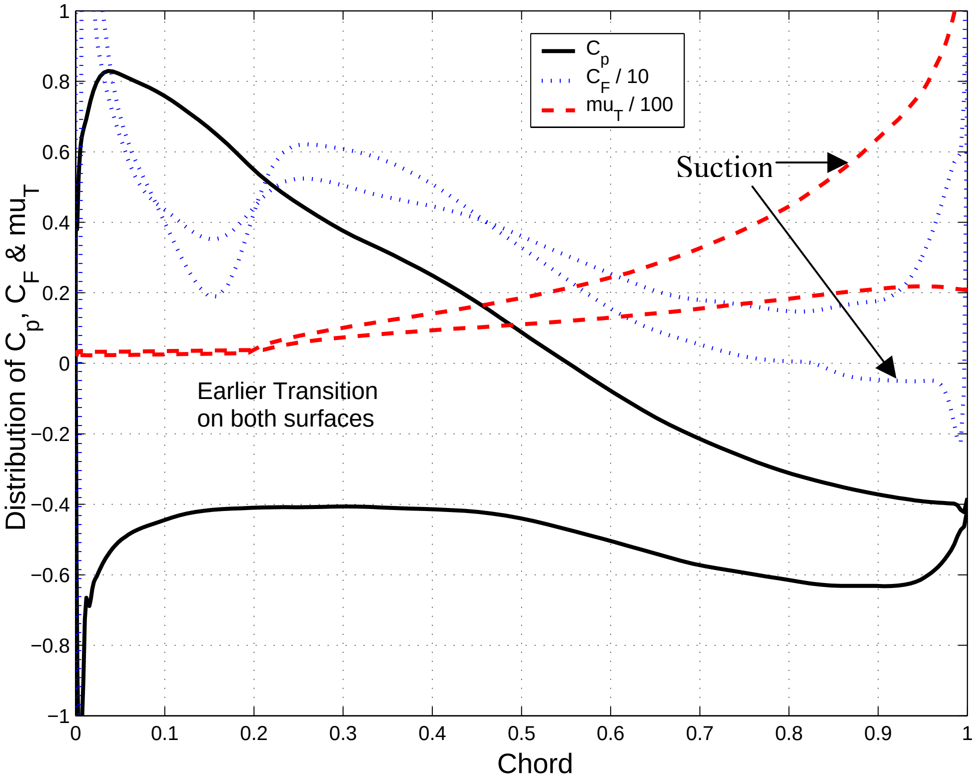

Figure 14. Separation / Transition Sensitivity Study: Distribution of Pressure Coefficient (C_p) Skin Friction (C_F) and Turbulent viscosity (μ_T or mu_T) - (Low Re/Low Tu)

5. Summary of Transition Model Sensitivity Study

Table 2 summarizes the resulting losses and turning for the four cases. Additionally a number of conclusions can be made form these simulations.

Table 2. Summary of transition simulation showing how predicted total pressure losses and turning are sensitive to changes in Reynolds number and free-stream turbulence.

High Turbulence	$\bar{\varpi} = 2.59$ $Turning = 24.1^{\circ}$	$\bar{\varpi} = 2.09$ $Turning = 24.6^{\circ}$
Low Turbulence	$\bar{\varpi} = 2.33$ $Turning = 24.07^{\circ}$	$\bar{\varpi} = 1.53$ $Turning = 25.1^{\circ}$
	Low Reynolds	**High Reynolds**

a. Both Reynolds number and free stream turbulence have significant effects on separation and transition. These events then have significant effects on total pressure loss and turning.

b. The k-ω turbulence model is capable of predicting changes in the location of transition as well as boundary layer growth. Additionally, transition itself appeared to be sensitive to prior separation. Further, the type of transition—bypass, natural, or separated flow—appeared to be reflected by these changes in predicted transition location.

c. Because the solution was sensitive to Reynolds number and free stream turbulence intensity, careful selection of these values during the numerical simulations was required. Specifically, low Reynolds number effects could unnecessarily complicate the calculations. Additionally, low turbulence is unrealistic in all but the first compressor blade row.

F. COATING SHAPES

A wide variety of coating thickness profiles near the airfoil leading edge are possible depending on the application process, the properties of the liquid coating, and the environmental drying conditions that the paint experiences. For this study it was useful to neglect the details of the coating process, while retaining the essential feature—the resulting degree of non-uniformity.

While possible shapes from the combination of factors are nearly infinite, a simplified model could represent the probable range of shapes resulting from uniformly applied films. Figure 15 shows the preliminary results of numerical simulations by Schwartz. It illustrates the final height of coating on a curved, base metal substrate using an initially uniform thickness application. It results from the selection of a single combination of the above factors.

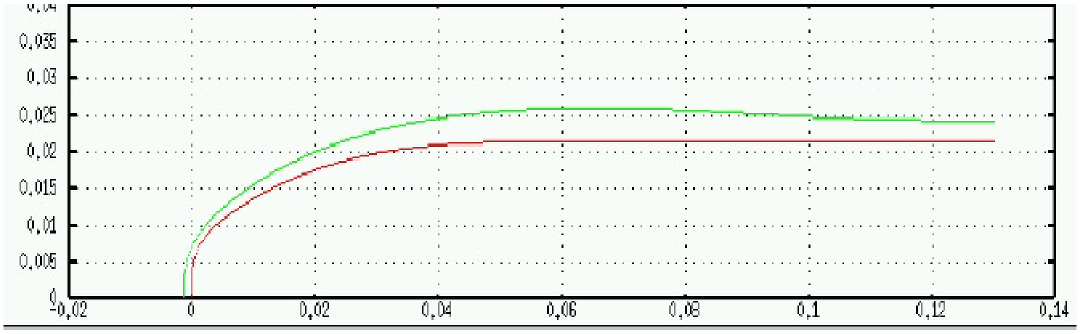

Figure 15. Numerical simulation of dried coating on a curved substrate using an initially uniform coating thickness. [From Schwartz, unpublished preliminary results]

In essence the degree to which the coating flows away from the leading edge can be represented by a degree of non-uniformity. This degree of non-uniformity is controlled by a single parameter, k and is represented by Equation 4. In this equation, k ranges from 0 to 1.

$$h(s) = h_0 - (0.5k) \cdot [s^{1.4} + 0.8(0.5k)^{1.2}] \cdot \exp[-0.5s(0.5k)^{-1.1}] \cdot \cos[.56s(0.5k)^{-1.4}] \quad (4)$$

Here, h is the coating thickness as a function of the arc length, s. Coating that dried uniformly would have a thickness h_o over the entire airfoil. Since the coating thickness is assumed to be one mil applied to a nominal four to five mil leading edge, h_o was set to 0.18 percent chord based on a leading edge radius of 0.666 percent of chord.

While the equation is complicated it represents a single parameter family of curves that covers a broad range of possible leading edge coating profiles. A k of zero represents a uniform coating. As k increases, coating at the leading edge thins while the shoulder height increases and moves away from the leading edge. A k of one represents a coating distribution with the dry coating height at the shoulder that is double the uniform thickness. For all values of k, the coating height decays to the uniform thickness, h_o, before the arc length, s, exceeds 5% chord. Figure 16 shows the family of curves generated by Equation 5 for k = 0, 0.25, 0.5, 0.75 and 1. The profiles represented by these thickness distributions cover the range of expected leading edge shapes that could form due to surface tension driven flows.

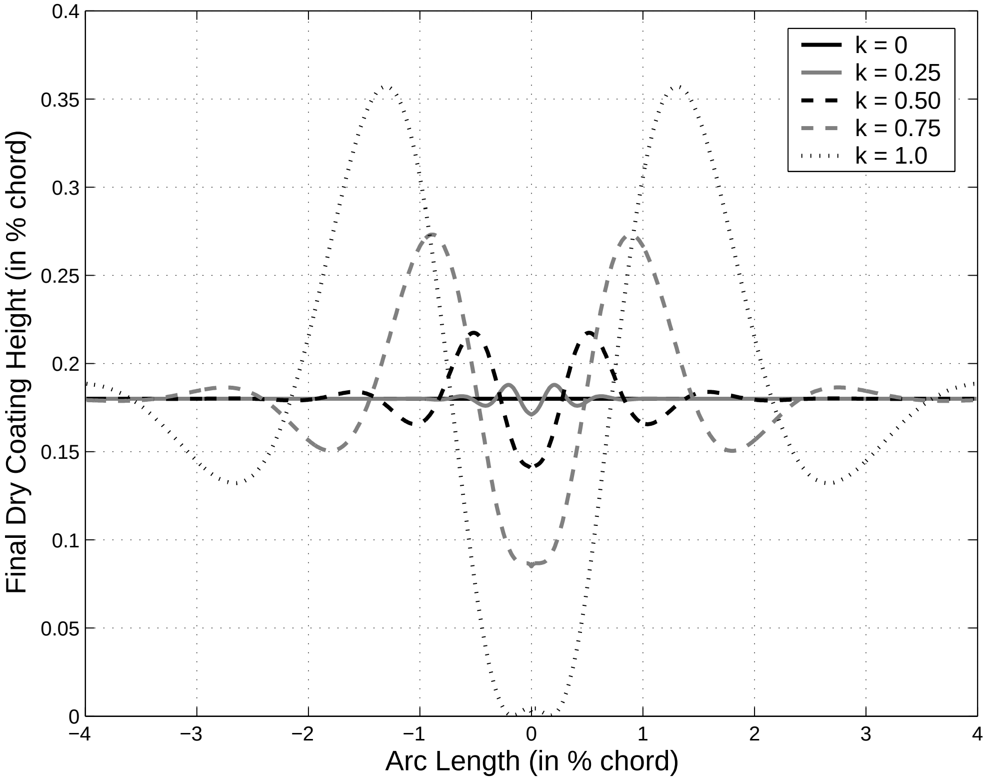

Figure 16. Family of Coating Curves: Coating thickness near leading edge

In reality, the curves should decay from the shoulder peaks to the uniform thickness without the undershoot shown in Figure 16. This difference was assessed to cause negligible changes to the final results.

These dry coating thickness heights were then added to the baseline airfoil coordinates using a MATLAB code shown in Appendix D. The resulting leading edge profiles are shown in Figure 17. Numerical integration of the area under the curves was used to ensure conservation of coating among the entire family of curves was within 2% of the uniform coating case. This calculation was conducted in the same MATLAB code. For this study, trailing edge thickness differences were ignored.

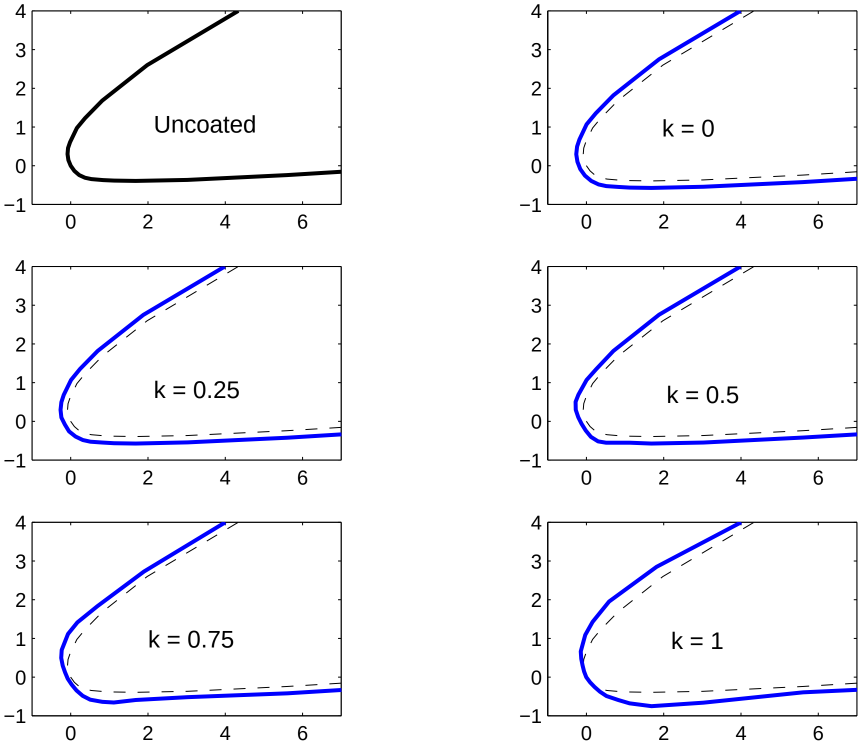

Figure 17. Leading Edge Profiles (scale is % chord).

The first plot in Figure 17 shows the base geometry. For the other five cases (k = 0, 0.25, 0.5, 0.75, and 1.0), the outer curve represents the coated profile and the inner base geometry is shown for reference. These six cases are used to study how coating non-uniformities at the leading edge of a compressor airfoil affect turning and total pressure losses at various Mach numbers and incidence angles.

III. RESULTS AND DISCUSSION

A. OVERVIEW

Numerical simulations were conducted for each of the six leading edge profiles over a range of Mach numbers and inlet air angles. First, the effect of the six coating profiles was examined at a single incidence and Mach number. Next, Mach number was varied from 0.6 to 0.8 for each of the profiles. Then for two inlet Mach numbers—0.6 and 0.75—the incidence was varied to determine off-incidence behavior for the different profiles. Table 3 summarizes the simulations conducted.

Table 3. Summary of Numerical Investigations.

Investigation	**Inlet Mach Number**	**Air Inlet Angle (degrees)**
Effect of Non-uniformity	0.6	45
Effect of Mach Number	0.6	45
	0.65	45
	0.7	45
	0.75	45
	0.8	45
Effect of Incidence (Subsonic Cases)	0.6	39
	0.6	40
	0.6	41
	0.6	42
	0.6	43
	0.6	44
	0.6	45
	0.6	46
	0.6	47
	0.6	48
	0.6	49
	0.6	50
Effect of Incidence (Transonic Cases)	0.75	40
	0.75	41
	0.75	41.5
	0.75	42.5
	0.75	43.5
	0.75	44
	0.75	45
	0.75	46
	0.75	47
	0.75	48
	0.75	49
	0.75	50.5

Simulations were conducted using a free-stream turbulence of 6% and a Reynolds number based on chord of 600,000. Stagger was set at 28.5° while solidity was set to unity. For each simulation, blade surface distributions of pressure, velocity, skin friction and turbulent viscosity were calculated. From energy averaged inlet and exit values, the total pressure losses and turning were determined using Equations 1 and 2.

B. EFFECT OF LEADING EDGE NON-UNIFORMITY

The initial simulation used an inlet Mach number of 0.60 and inlet air angle of 45°. Figure 18 shows the pressure coefficient (C_p) distribution around the airfoil.

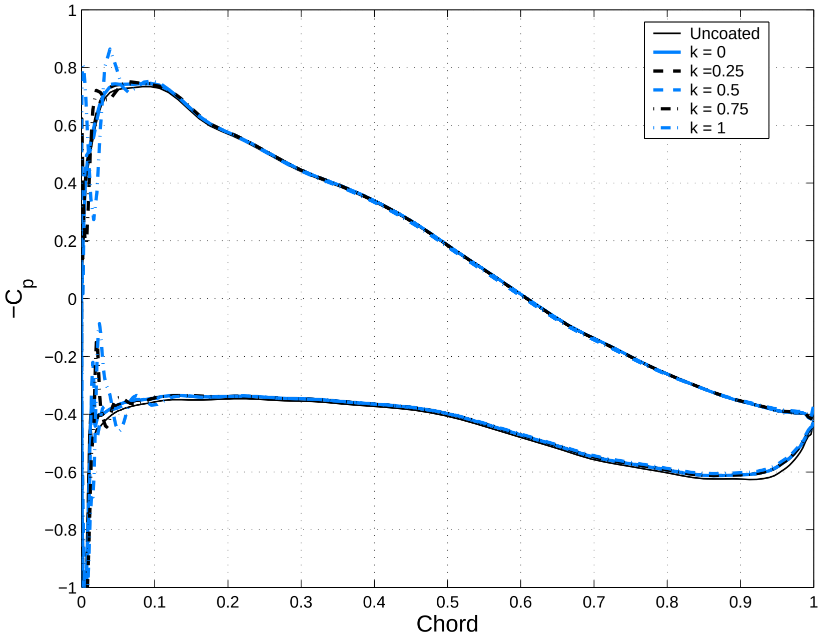

Figure 18. Pressure Coefficient Distribution versus chord for various coating non-uniformities. 45 degree air inlet and Ma = 0.6.

Figure 19 more closely examines the suction side leading edge region through 15% chord. The uncoated airfoil represented by the thin dotted line shows a smooth distribution of C_p just below the coated curves. The distributions for k = 0 and k = 0.25 are both smooth and lay just above the uncoated curve. For k = 0.5 two small C_p overshoots occur as the velocity climbs up to the maximum velocity plateau. For the k = 0.75 case and the k = 1 case especially, a large over speed occurs at the leading edge, followed by a sharp deceleration and acceleration. Similar distributions occur near the leading edge of the pressure surface. Based on skin friction distributions, a short pressure side separation bubble for the k = 0.75 case occurs around 2.5% chord. The k = 1 case has a short separation bubble on the pressure side from about 3-5% chord. Based on turbulent viscosity distributions, all cases except k = 1 transition to a turbulent boundary layer between 17-19% chord on both surfaces. For the k = 1 case, transition begins on the pressure side at about 4% chord and on the suction side at about 17% chord.

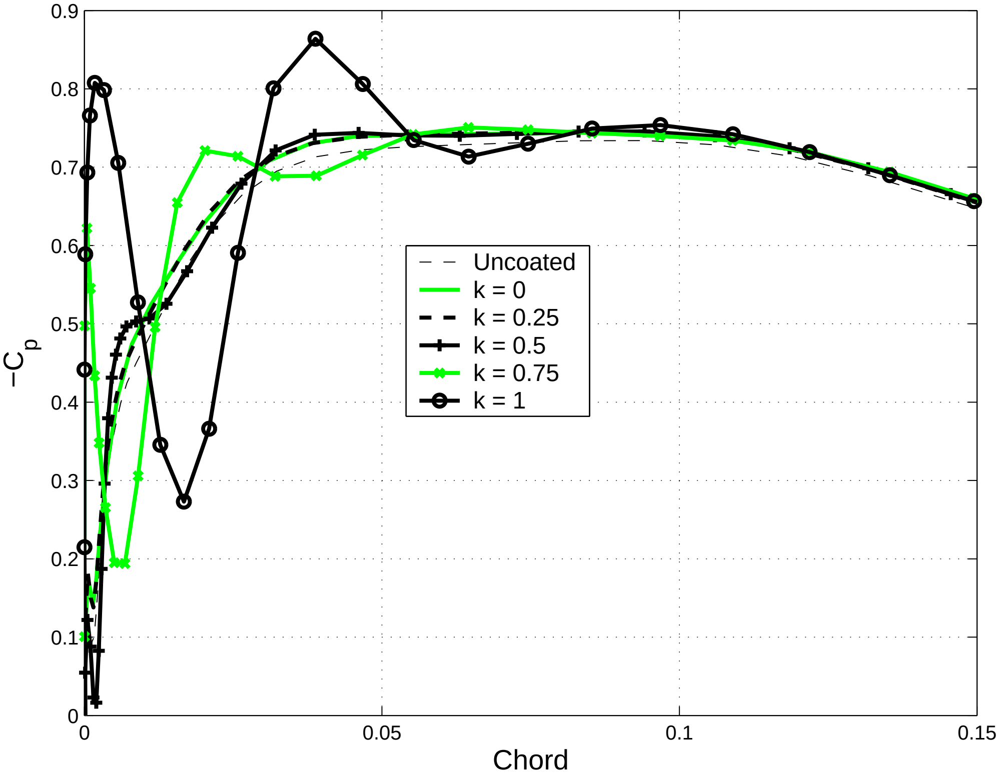

Figure 19. Suction surface pressure coefficient—first one-quarter chord. Various coating profiles at 45 degree inlet angle and Ma = 0.6.

Figure 20 shows how total pressure losses and turning vary with the non-uniformity parameter, k. The figure shows that losses increase for all coating profiles with increasing losses for the most non-uniform profiles. Turning decreases in a similar pattern. The losses and turning for the uncoated airfoil are shown for reference.

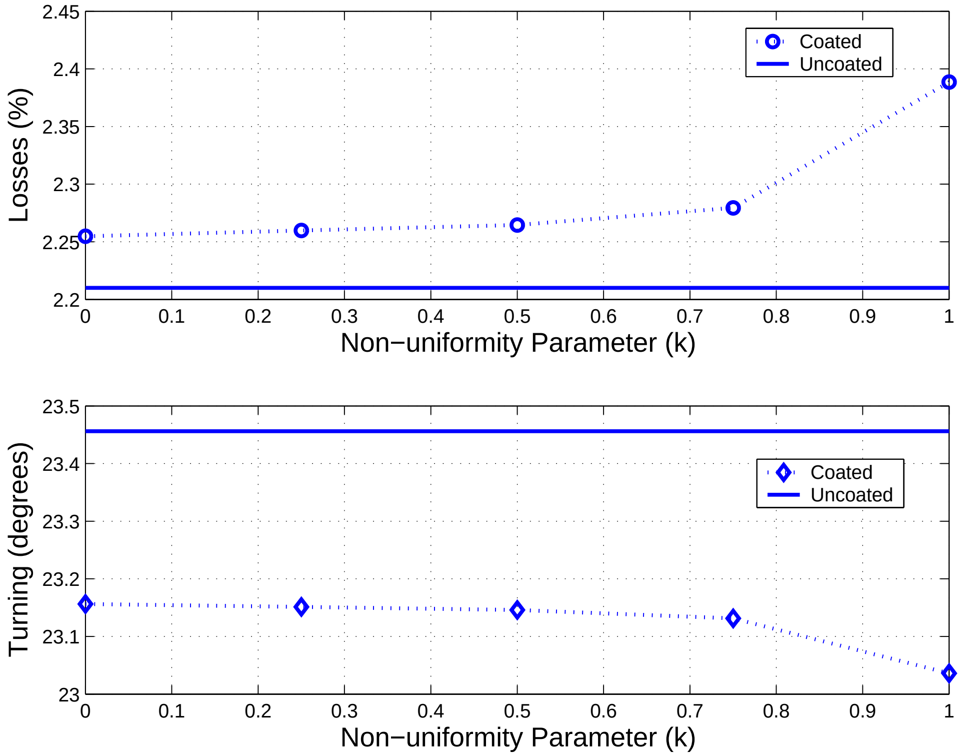

Figure 20. Total Pressure Losses $(\bar{\varpi})$ and Turning versus non-uniformity parameter (k): For $\alpha = 45$ and Ma = 0.6.

Figure 20 indicates that there is a 2% penalty in relative total pressure loss due to the addition of a uniform coating. At least two explanations could account for this increase. First, the increased losses could be due to the 25% increase in leading edge radius. Unpublished studies by Carter in 1961 and presented by Cumpsty [40] suggest losses increase with leading edge radius. Another physically intuitive explanation is due to the increased thickness of the airfoil. For this generic airfoil, thickness is nominally 10% of chord. A uniform coating on both surfaces results in a 10.36% thickness for a relative increase of about 4%. The increased thickness could increase overall drag and thus total pressure loss.

C. EFFECT OF INLET MACH NUMBER

The effect of Mach number at near zero incidences was examined for five cases as shown in Table 4.

Table 4. Mach Number Effect Simulation Runs

Mach Number	Pressure Ratio	Inlet Air Angle
0.60	0.881	45
0.65	0.868	45
0.70	0.854	45
0.75	0.840	45
0.80	0.826	45

Increasing Mach number tended to increase total pressure losses for the airfoil. For inlet Mach numbers of 0.75 and 0.8, a normal shock occurs, which further increases losses. In general, separation and transition locations follow those described for the Mach 0.6 case discussed above. Figure 21 shows how the losses and turning for the various profiles change with increasing Mach number. From Figure 21, losses increase as inlet Mach number approaches unity.

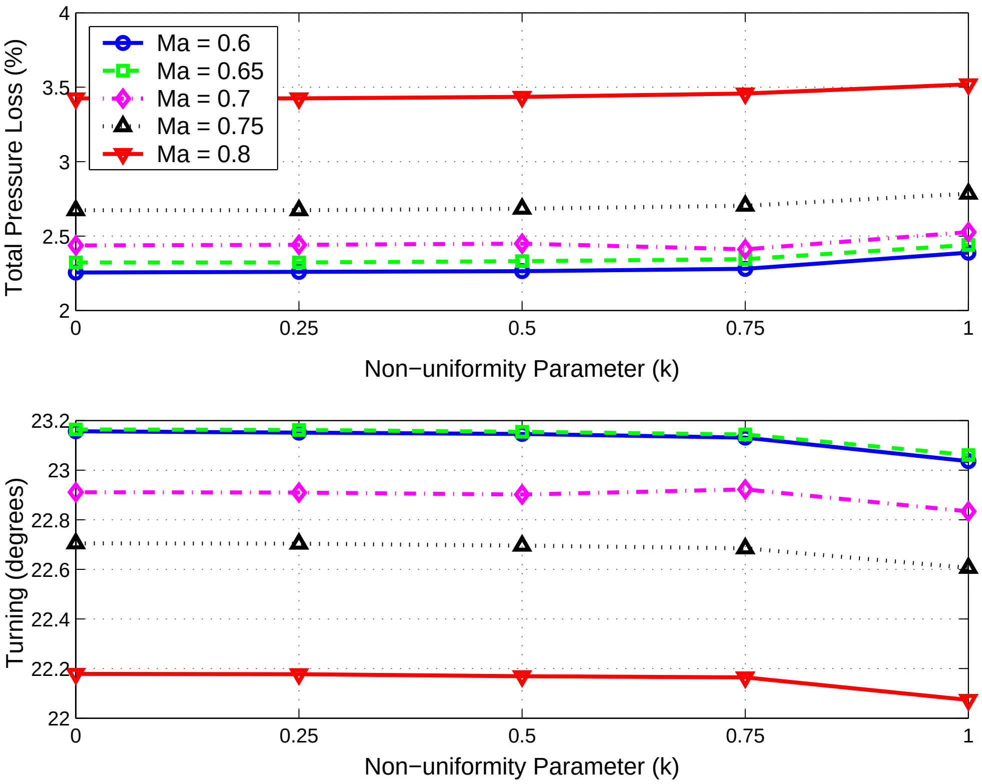

Figure 21. Losses and turning versus non-uniformity for various inlet Mach numbers

Figure 22 shows losses and turning normalized with the uncoated airfoil values. This shows how the previously studied effect of the coating profile changes with increasing Mach number. Again, the 2% relative increase in total pressure loss is visible. In general, both the total pressure loss and turning curves versus k follow the same pattern as Mach number is increased. However, the rise in losses from k = 0.75 to k = 1.0 is slightly shallower for the cases with a shock, $Ma \geq 0.75$. Curiously, for the Ma = 0.7 case, Figure 22 shows a slight improvement in losses versus k at k = 0.75. This improvement cannot be readily explained through by the pressure coefficient distributions. Figure 23 illustrates the cause of the predicted change. Based on turbulent viscosity distributions, transition for the k = 0.75 case is predicted to occur slightly downstream of that for the k = 0.5 case. The only visible explanation is that the velocity for the k = 0.75 case decreases more gradually in the vicinity of the suction side transition.

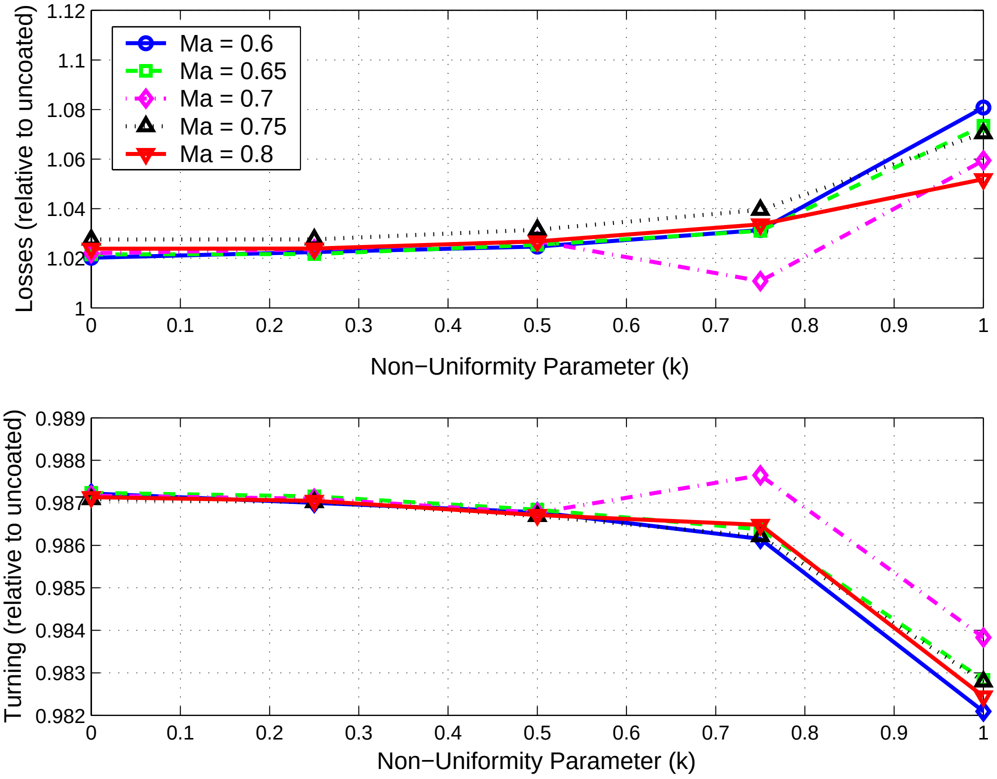

Figure 22. Normalized Losses and Turning versus K for various inlet Mach Numbers.

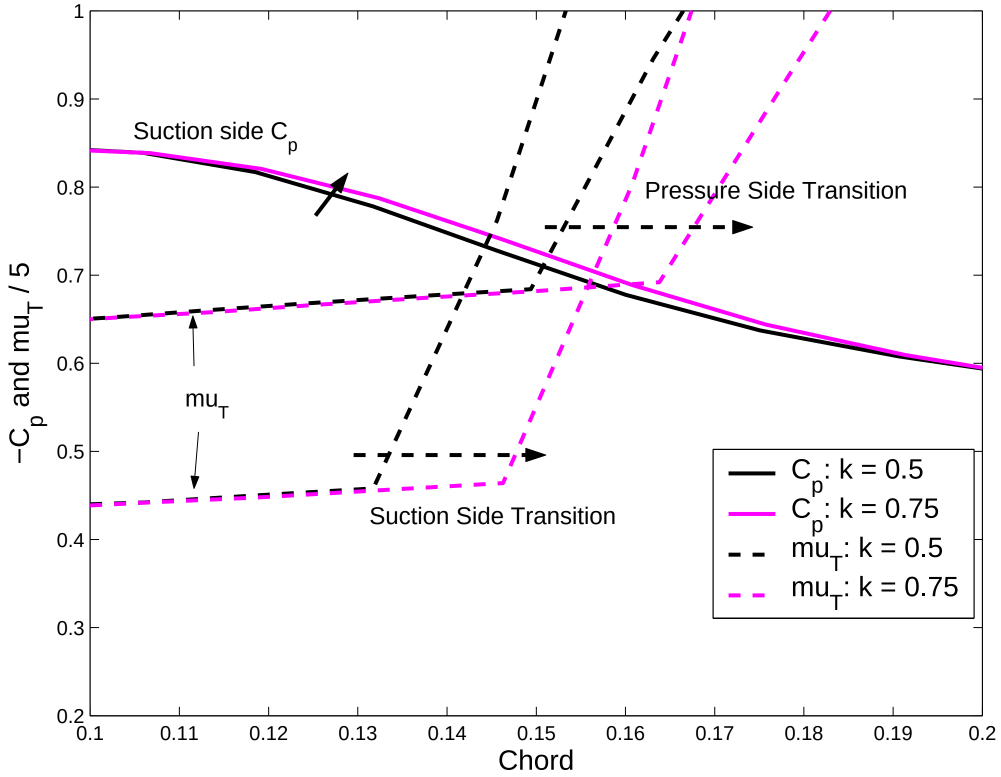

Figure 23. Suction Side Pressure Coefficient Distribution (Ma = 0.7) and Turbulent Viscosity (μ_T or mu_T) to show why losses for k = 0.75 decrease from k = 0.5

Figure 24 shows how the suction side leading edge pressure coefficient varies with inlet Mach number for the most non-uniform profile (k=1). In this figure, the peak grows, and as inlet Mach reaches 0.75, moves aft. There are two leading edge velocity spikes associated with each profile. The first occurs at 1% chord and the second occurs around 5% chord. The second spike gets nearly masked by the velocity rise for the Ma = 0.75 and 0.8 cases. This may contribute to the shallower loss penalty from k = 0.75 to k = 1 as seen in Figure 22.

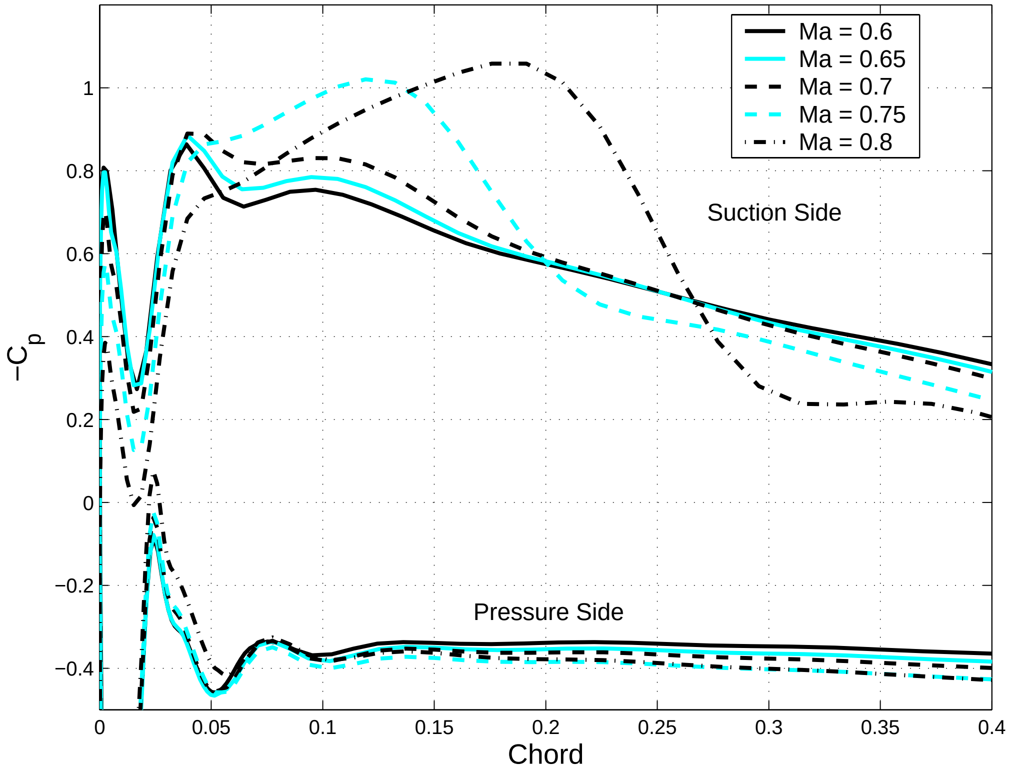

Figure 24. Shift in Pressure Coefficient with Mach for k = 1.

Something not shown above and not reflected in the losses is the occurrence of a suction side separation bubble at higher Mach numbers. For example, a small bubble forms at 0.7 to 0.9% chord on the suction side as shown in Figure 25. However, this bubble did not result in early turbulent transition of the boundary layer. Table 9 in Appendix E shows the results from these Mach number effect simulations.

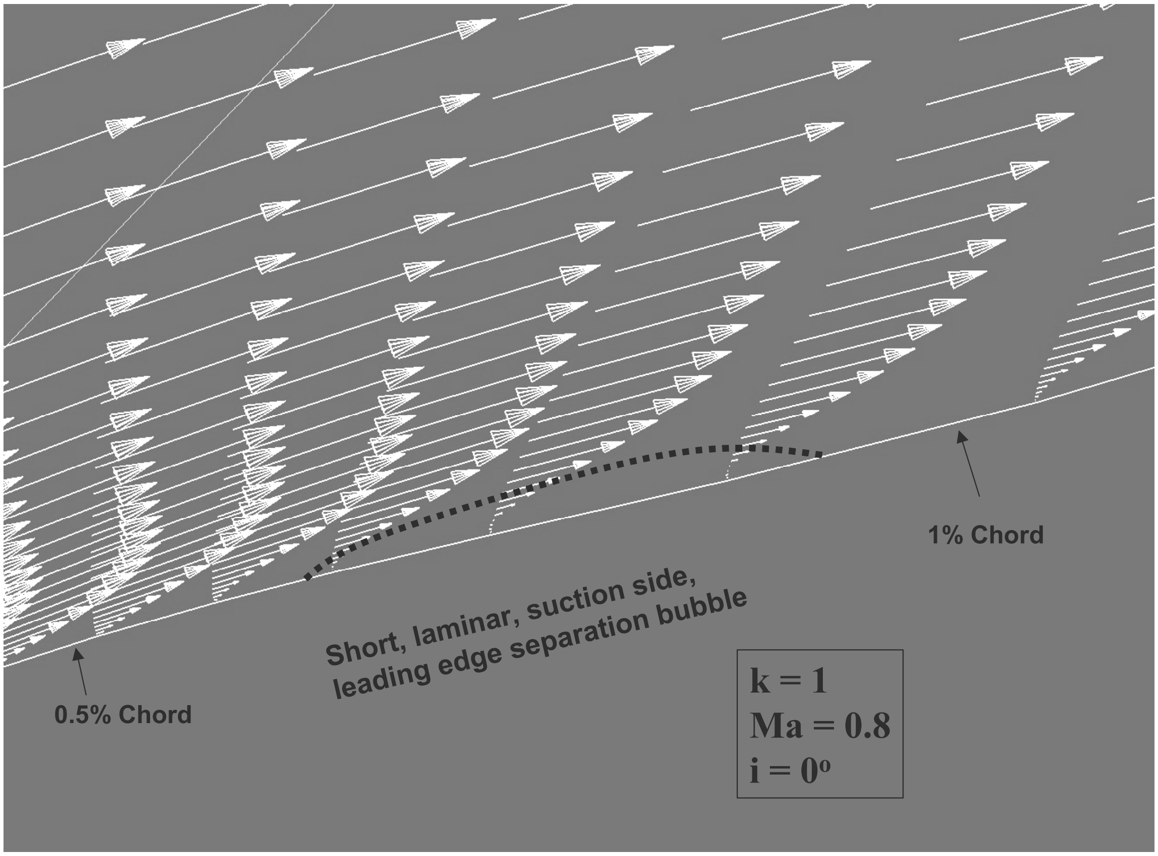

Figure 25. Separation Bubble that formed near leading edge of suction surface for Ma = 0.8 and coating parameter, k = 1.

D. EFFECT OF INCIDENCE

1. Subsonic Cases

Incidences from approximately –6 to +6 degrees were simulated at an inlet Mach number of 0.6. Table 5 summarizes the inputs for the simulations used to study the effect of incidence. Again, for each of these cases, data was acquired for all six leading edge profiles. Tables 10 and 11 in Appendix E display the results for these cases.

Table 5. Incidence angle effect simulation runs (Ma = 0.6)

Inlet Air Angle	Mach Number	Pressure Ratio
39.3	0.6	0.856
40.3	0.6	0.861
41.2	0.6	0.865
42.1	0.6	0.869
43.1	0.6	0.873
44.0	0.6	0.877
45.0	0.6	0.881
46.2	0.6	0.886
47.1	0.6	0.890
48.1	0.6	0.894
49.2	0.6	0.898
50.3	0.6	0.902

As incidence is increased slightly from 45° to 46° the pressure side laminar separation bubbles for the k = 1 and k = 0.75 cases disappear. Losses for these two cases drop while the remaining cases increase slightly. As incidence continues to increase, suction side separation bubbles begin to form. These bubbles form first on the k = 1 case followed by the k = 0.75 case. Additionally, as incidence increases, turbulent separation moves forward from near the trailing edge at 93% chord to about 80% chord. When the air inlet angle reaches 50°, the k = 1 case suction side boundary layer separates and quickly transitions to turbulence between 0.2-2.2% chord with massive turbulent separation occurring at 34% chord. The early separation bubble leading to early transition to turbulence is shown in Figure 26. The suction side boundary layer for the k = 0.75 case also separates at 0.2% and reattaches turbulently at 12% chord. Deviation grows as incidence increases. This appears to mainly be due to turbulent separation moving forward from near the trailing edge.

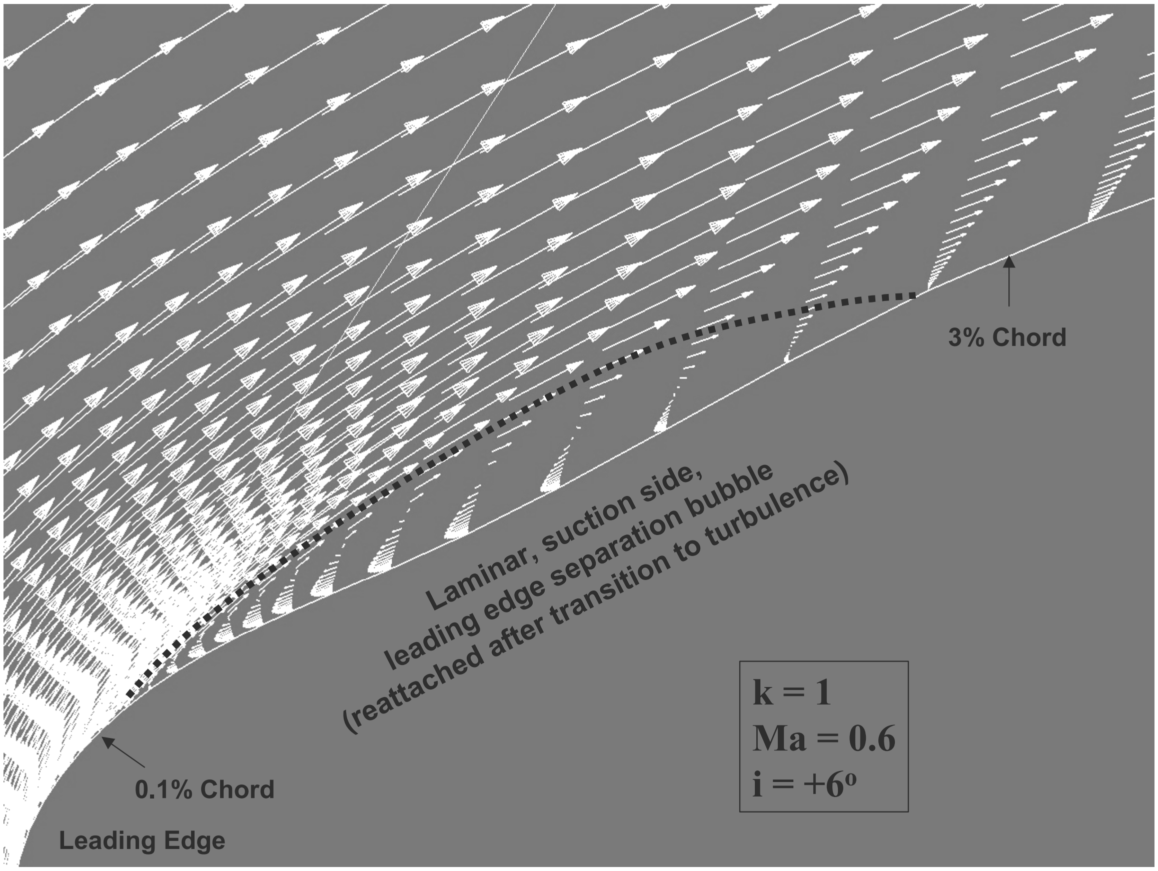

Figure 26. Separation Bubble on Suction side that reattached after transition to turbulence for Ma = 0.6, Air Angle of 50 degrees and k = 1.

As inlet air angle is decreased from 45° to negative incidences, losses slowly climb. Below 44°, pressure side boundary layers begin to separate beginning with the more non-uniform airfoils first. Pressure side transition to turbulence also moves forward resulting in greater total pressure losses. Pressure side separation occurs for all profiles below 40.5°. In general, the growth in total pressure loss is more rapid as the leading edge non-uniformity increases. Deviation for all profiles gets slightly smaller as the air angle decreases and less turning is required. Deviation for the uncoated airfoil is consistently a half-degree better than the coated cases. If a bulbous trailing edge had been generated, this deviation penalty may increase further.

Figure 27 shows the summary of total pressure loss $(\bar{\varpi})$ and deviation (δ) versus inlet air angle at Ma = 0.6. This figure begins to form "loss buckets" showing losses as a function of incidence for each profile.

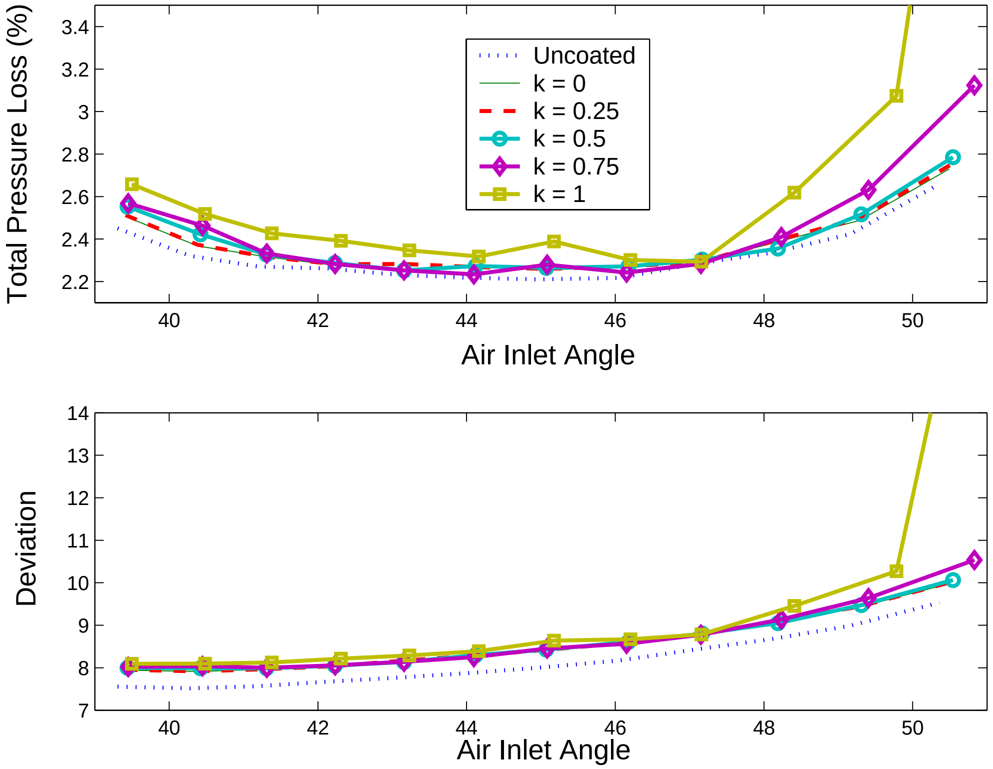

Figure 27. Total Pressure Loss and Deviation versus Inlet Air Angle at Ma = 0.6.

2. Transonic Cases

Next, incidences from approximately –6 to +7 degrees were simulated at an inlet Mach number of 0.75. Table 6 shows the input parameters for the simulations used to study the effect of incidence. Tables 12 and 13 in Appendix E show the results for these cases.

Table 6. Incidence angle effect simulation runs (Ma = 0.75)

Inlet Air Angle	Mach Number	Pressure Ratio
40.3	0.75	0.814
41.0	0.75	0.816
41.6	0.75	0.820
42.5	0.75	0.826
43.5	0.75	0.832
44.3	0.75	0.836
45.1	0.75	0.840
46.0	0.75	0.844
47.0	0.75	0.848
48.3	0.75	0.853
49.4	0.75	0.855
50.9	0.75	0.856

As inlet air angle increases above 45°, losses for all profiles grow rapidly. From the pressure coefficient distribution, the velocity peak gets larger and moves forward on the airfoil. This generates a stronger shock that moves forward with incidence. Boundary layer transition is driven by the shock and thus moves forward also. Figure 28 shows the effect of incidence on the suction side pressure coefficient.

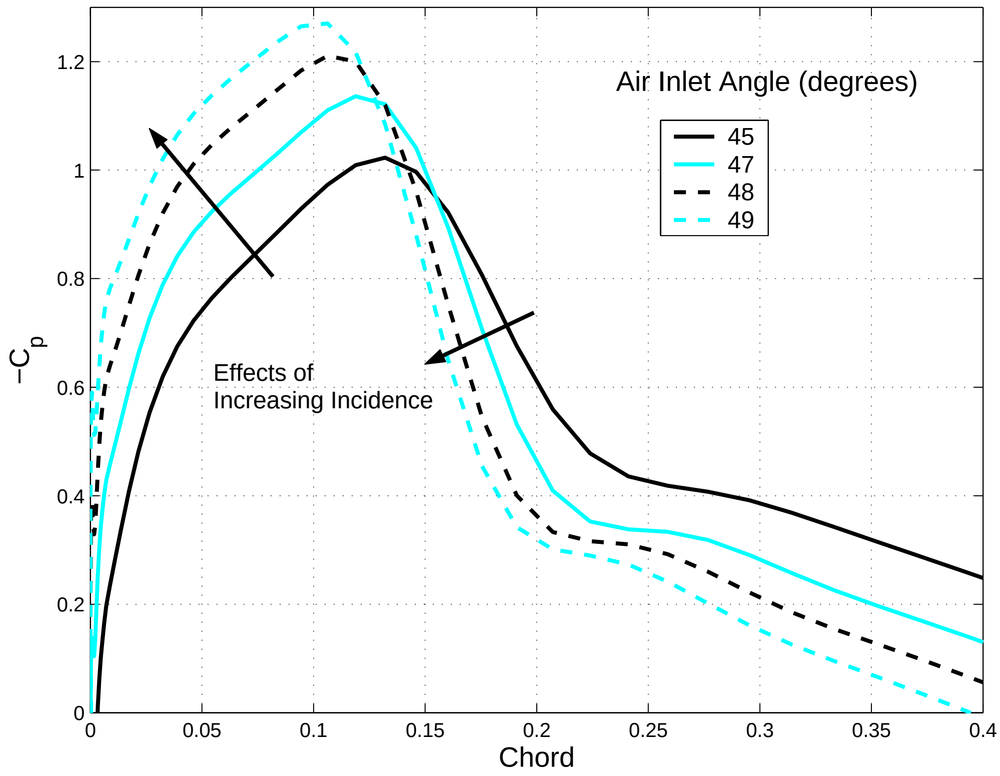

Figure 28. Suction Side Pressure Coefficient at four increasing inlet angles for uncoated airfoil at Ma = 0.75.

At high incidence $(\sim 49^{\circ})$, an early lip shock appeared on the suction side leading edge for the k = 1 profile. This early shock reduced the severity of the normal shock at about 20% chord. Overall, losses for this profile fell below the other cases. Figure 29 shows the double shock for the k = 1 case compared with the single sharp shock for the k = 0 case. Above 50° inlet air angle, all of the profiles undergo separation and rapid transition to turbulence between 10 and 15% chord. As in the Ma = 0.6 cases, trailing edge turbulent separation occurred earlier as positive incidence increased.

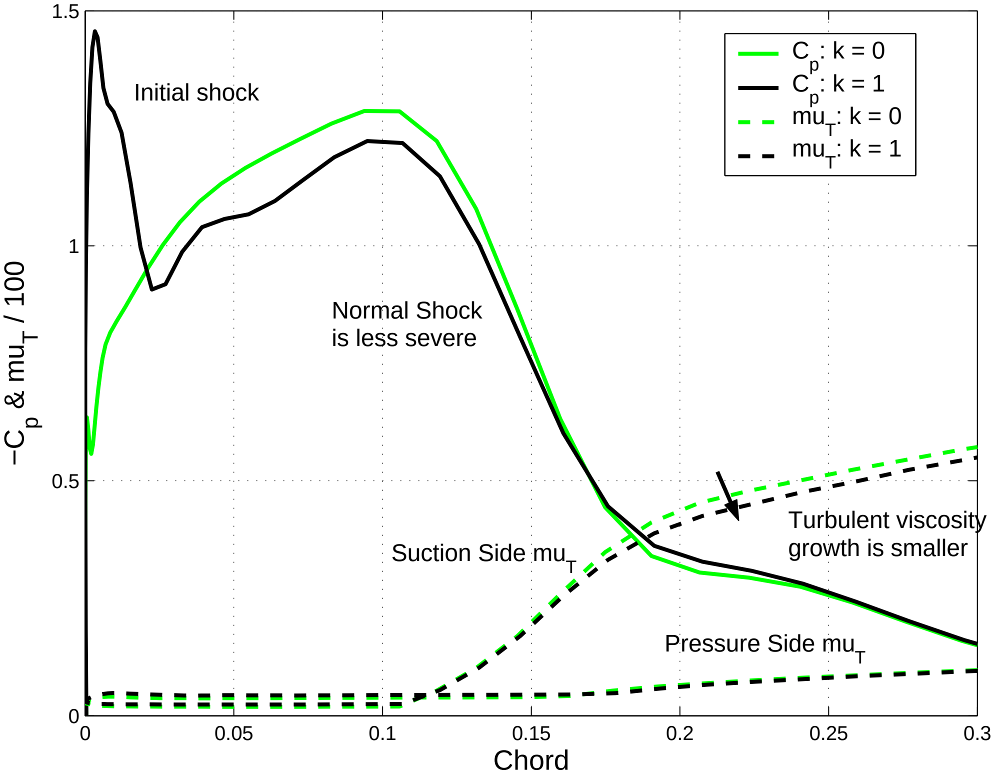

Figure 29. Suction Side Pressure Coefficient and Turbulent Viscosity (μ_T or mu_T) showing leading edge shock at 49 degree inlet angle and Ma = 0.75.

At air angles less than 45°, laminar separation bubbles begin to form on the pressure side similar to the 0.6 Mach number cases. Below 45°, separation occurs for k = 0.5 to k = 1. The separation bubbles result in rapid turbulent transition for the k = 1 case. The code predicts that they reattach as laminar boundary layers for the other two profiles. Below 42°, pressure side separation bubbles had formed for all profiles. The tendency of the laminar bubble to transition to turbulence seemed to increase with increasing coating non-uniformity. By 40°, pressure side leading edge separation bubbles led to prediction of early turbulent transition for each profile. Figure 30 shows the results of total pressure loss $(\bar{\varpi})$ and deviation (δ) versus inlet air angle for an inlet Mach number of 0.75.

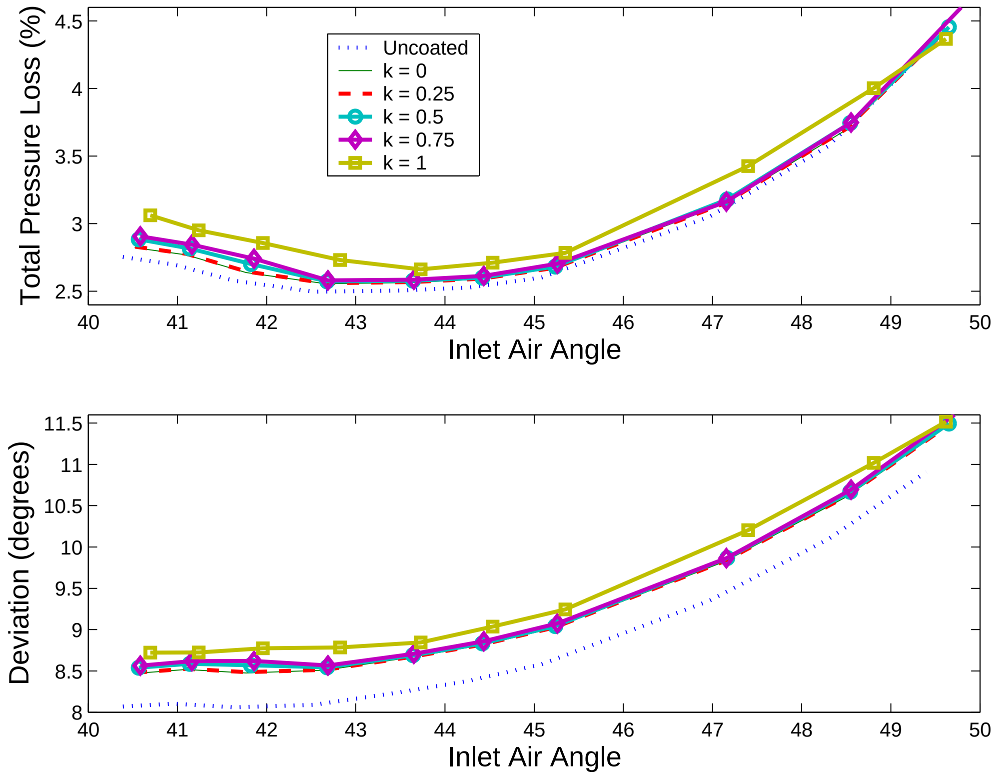

Figure 30. Total Pressure Loss and Deviation versus Inlet Air Angle at Ma = 0.75

E. DISCUSSION

The CFD simulations show that there is a total pressure loss and deviation penalty due to the addition of a non-uniform coating. At low incidence, the worst case coating (k=1) total pressure losses are nearly 5% greater than the uniform coating and 8% greater than the uncoated airfoil. As incidence is increased, these penalties tend to increase. For the 0.6 Mach case, massive turbulent separation occurs at lower positive incidences as the k parameter increases. For the higher Mach number case, however; a shock close to the leading edge occurs for the k=1 case at high positive incidence that appears to diminish the losses from the larger shock that occurs at 20% chord for each of the cases. The result is that losses converge at higher incidences for the higher Mach number simulations.

In general, increasing the non-uniformity of the coating has an effect similar to increasing Mach number (as seen in NASA SP-36 [41]) in that total pressure loss buckets become narrower. Similarly, off-incidence effects are magnified by the non-uniform leading edge.

Computations show that the application of a non-uniform coating affects separation and transition. As the non-uniformity is increased, velocity spikes appear on the C_p distribution. In some cases, these spikes cause adverse pressure gradients that are severe enough to cause leading edge separation bubbles. Separation can then lead to predicted boundary layer transition. In other cases, the observed velocity spikes drive predicted boundary layer transition without separation. In general, these cases result in predictions of higher total pressure losses and reduced turning.

However, in some cases where separation occurs, the CFD code does not predict transition to turbulence prior to bubble reattachment. This is contrary to the results of Tain [17] and Walraevens and Cumpsty [16] where observed leading edge separation bubbles resulted in transition to turbulence. The low Reynolds number k-ω turbulence model combined with the thin-layer Navier Stokes equations may be limited. A better turbulence model for predicting transition in a separation bubble may need to include a shear stress transport (SST) model such as the one developed by Menter [42]. Another possibility is that small-scale three-dimensional effects may drive transition in the separated shear layer. If so, a three-dimensional flow solver may better predict conditions downstream of a separation bubble.

On the other hand, many of the separation bubbles predicted in this study occur due to curvature discontinuities. As the flow continues past the shoulder bump, a very favorable pressure gradient may allow relaminarization upon reattachment of the boundary layer. According to Gostelow [2], “Usually but not always, the bubble acts somewhat as a trip wire and promotes rapid transition to turbulence.” Further empirical study and numerical simulation—perhaps through direct numerical simulation (DNS) or a 3D solver—is needed to determine actual transition locations.

Another potential problem is grid independence for the more non-uniform leading edges at higher incidence conditions. The grid resolution study was conducted at near zero incidence on an uncoated airfoil. More chord-wise points near the leading edge may be needed to resolve transition of the separation bubbles that form under conditions of high incidence and coating non-uniformity.

Since leading edge separation bubbles should typically lead to early transition to turbulence, the presence of these bubbles can be considered as an impact to aerodynamic performance. To investigate the occurrences of leading edge separation, each occurrence has been plotted. Figure 31 shows the regions where separation—either suction or pressure side—was predicted. This two-dimensional map of inlet angle versus non-uniformity also includes the effect of two different Mach number cases. In the upper right corner, suction side separation is predicted while the lower right corner shows where pressure side separation is predicted. The remaining regions represents predicted attached flow.

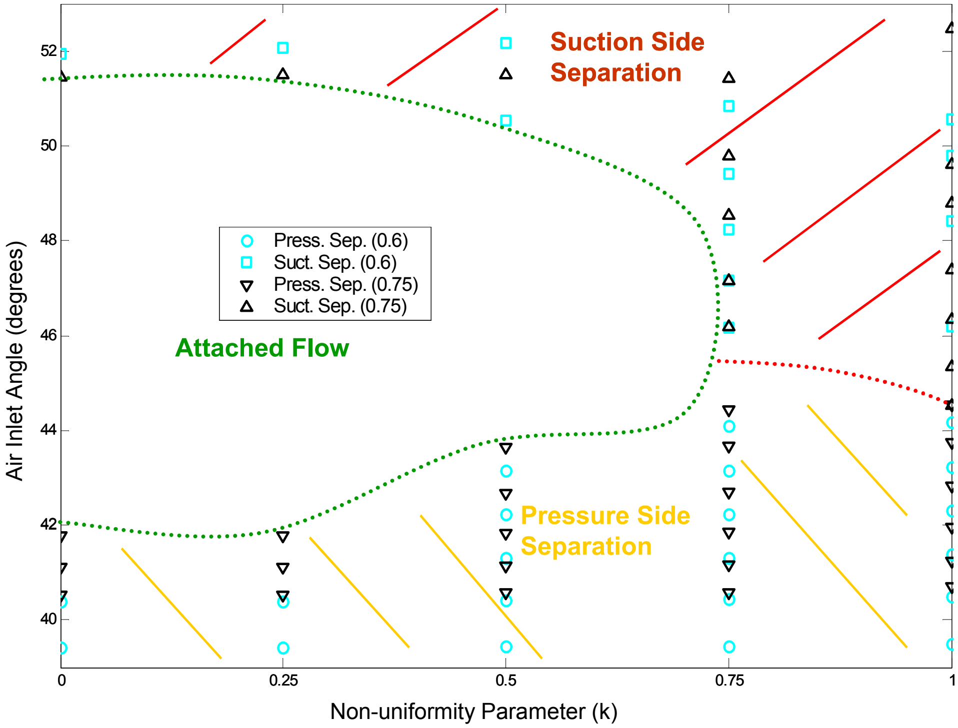

Figure 31. Map of Leading Edge Separation Regions: Shows cases with boundary layer separation for a given air angle, Mach number and coating parameter (k).

Tuck [17] developed a criterion for leading edge separation. He found that suction side separation occurs when the incidence angle,

$$i > 0.818(r/c)^{1/2} \tag{6}$$

where i is incidence in radians, r is leading edge radius, and c is chord. This equation assumes a thin airfoil with a smooth leading edge that can be modeled as a parabola in incompressible flow. The present study used a cambered airfoil with a circular leading edge in compressible flow. Coating non-uniformities further altered the quasi-parabolic nose. For the NACA 65 (12)10 with a uniform one mil coating, Tuck's criterion predicts separation at:

$$0.818\left(\frac{r}{100}\right)^{1/2}\frac{180^\circ}{\pi} \approx 4.3^\circ \tag{7}$$

where r = 0.666 (nominal leading edge radius) + 0.18 (coating) = 0.846.

In this study, suction separation first occurred between 49.6 and 51.4 degrees while pressure side separation first occurred between 42.65 and 41.8 degrees on the uniformly coated airfoil. This shows separation at $\pm 4.2^\circ$ from 46.4°, a difference from Tuck's incompressible prediction of about 2%. As Mach number and the k parameter are increased, data from the incidence angle effect simulations shows earlier separation. By making an adjustment to Tuck's criterion, the effects of Mach number and coating non-uniformity can be fit to the data. In the present study, separated flow is predicted when:

$$|i| > 1.2\left[\left(\frac{r}{c}\right)^{0.5} - A(k)^B\right]\sqrt{1 - Ma^2} \tag{8}$$

where i is incidence in radians, k is the coating shape factor defined by equation (4), r is the leading edge radius, c is chord length and Ma is inlet Mach number.

In order to match the computed results, the constants, A and B, have been set to 0.3 and 4.0 for suction side separation and 0.15 and 2.0 for pressure side separation as shown in Figure 32. Mach numbers are shown in the legend (0.6 or 0.75) and indicate a smaller region of attached flow as inlet Mach number increases.

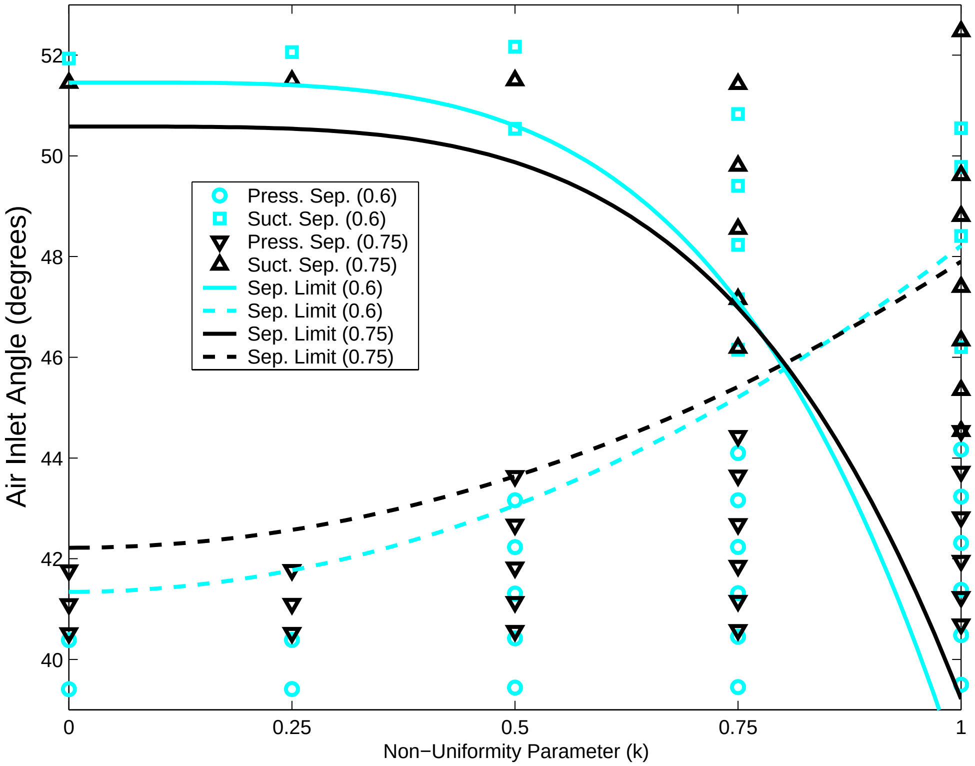

Figure 32. Map of Leading Edge Separation Regions with correlation curves accounting for incidence, Mach number and non-uniformity (k).

This map of separation regions reveals a level of aerodynamic impact as a function of the leading edge non-uniformity. First, it shows that for k ≤ 0.25, there is no effect on separation. Between k = 0.25 and k = 0.5, the incidences resulting in a leading separation bubble increase. By k ≥ 0.75, a leading edge separation bubble results for nearly all incidences. Based on these predictions, the aerodynamic impact of increased probability of separation first occurs between k = 0.25 and k = 0.5. Therefore, in order to avoid an increased probability of separation, the coating shoulder height should be kept less than 20% above the uniform thickness. This could be accomplished by changing the formulation and/or application of the coating.

F. IMPACT OF LOSS ON ENGINE PERFORMANCE

The predicted increase in aerodynamic losses for a single compressor cascade will affect overall engine performance. Three gas turbine engine performance measures—specific fuel consumption, power, and starting times—can be assessed.

By estimating the penalty in specific fuel consumption (SFC), the economic impact of the leading edge non-uniformity can be assessed. From the computed two-dimensional total pressure losses and turning, a specific fuel consumption (SFC) penalty could be calculated as:

$$\Delta SFC(\%) = C_1 \cdot \left(\frac{\varpi_c - \varpi_{uc}}{\varpi_{uc}} \right) + C_2 \cdot \left(\delta_c - \delta_{uc} \right) \tag{9}$$

Where $C_1 = \left[\frac{\text{\% SFC}}{\text{\% increase in total pressure loss}} \right]$ and $C_2 = \left[\frac{\text{\% SFC}}{\text{decrease in }^{\circ}\text{turning}} \right]$.

It can be shown by relating cascade losses and turning to stage efficiency, compressor efficiency, and finally overall thermal efficiency using equations from Hill and Peterson [43] that $C_1 \approx 8$ and $C_2 \approx 0.5$. The values for C_1 and C_2 are rough approximations and were obtained by selection of typical naval gas turbine parameters. Figure 33 illustrates the SFC penalty from Equation 9 as a function of incidence and non-uniformity.

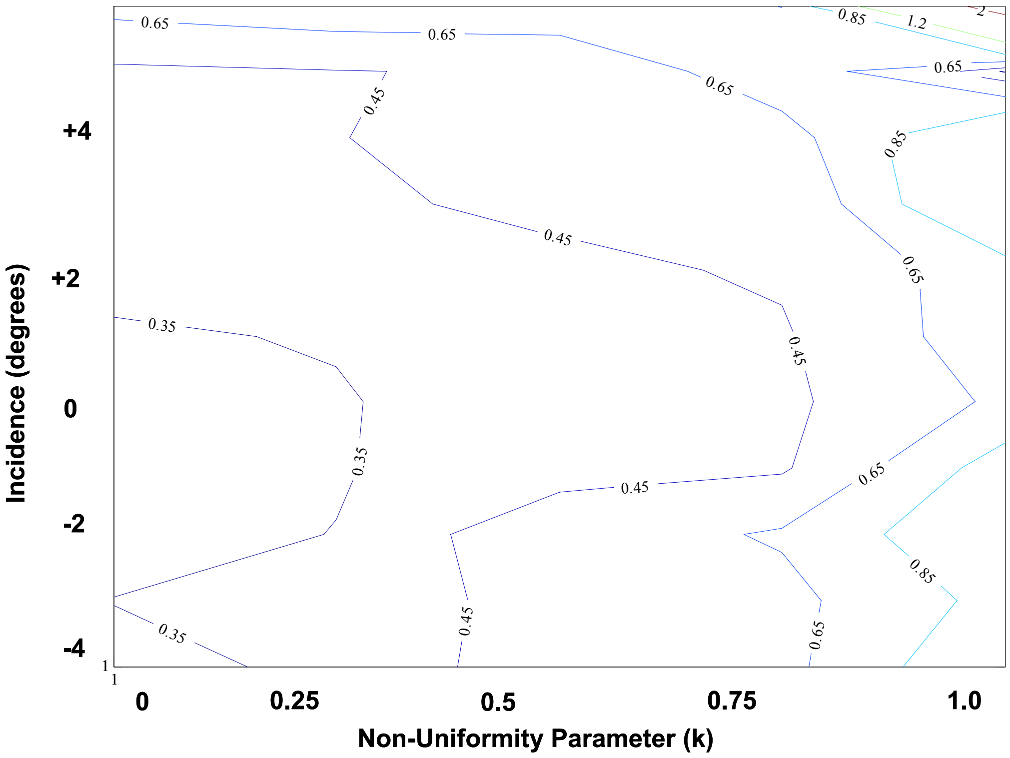

Figure 33. Contour plot of additional %SFC for an applied coating profile (k) and incidence. (Ma = 0.75)

Like the map of separation, Figure 33 indicates increased SFC as either non-uniformity or the absolute value of incidence increase. Also from this graph, the non-uniformity appears to enhance the off-incidence penalty. Here, a measurable increase in SFC occurs at about k = 0.5.

A second measure of overall machine performance is power generation. Clearly, specific power output would be reduced for the non-uniform leading edge profiles. Additionally, mass flow rate could also be reduced due to the degraded leading edges resulting in a reduced total power output.

For many applications such as naval propulsion, machine startup time is a very important performance measure. During startup, flow within the compressor will be highly off incidence until the pressure ratios and thus densities reach steady design values. Incidences will be positive at early stages and highly negative at later stages. From Figure 31, the greater leading edge profile non-uniformities result in a smaller range of incidence that allows attached flow. A possible result is increased starting times as interstage bleed is used to try to match design incidence.

The assessment of three key measures of overall gas turbine engine performance indicate a significant impact to performance due to non-uniform leading edge profiles. Coating formulation and application methods should be controlled such that these negative impacts are managed. Additionally, the impact of non-uniform leading edges from manufacture would be expected to cause similar performance penalties. This impact assessment could also be used when designing and manufacturing airfoil leading edges.

IV. CONCLUSIONS

The validated, quasi-three dimensional Navier-Stokes code, RVCQ3D, was used to predict the impact of coating non-uniformity on total pressure loss and turning for a two-dimensional compressor cascade. From this study, several conclusions were made.

(1) The CFD code was capable of calculating flow conditions that matched the selected cascade testing empirical data.

(2) The k-ω turbulence model's predictions of separation and transition are sensitive to changes in flow conditions. However, numerous cases predicted separation bubbles that did not result in transition to turbulence. RVCQ3D using the k-ω turbulence model may not be able to model properly the transition of flow within a separation bubble. A SST model such as that by Mentor may better predict this transition. The code used in this study is assessed to be able to predict the occurrence of a leading edge separation bubble, but not always the behavior of the boundary layer downstream.

(3) The total pressure losses and turning (or deviation) have been calculated numerically for various Mach numbers and over a range of incidences. For nearly every case, both losses and deviation increased as coating profiles became less uniform. These relative changes in losses as a function of non-uniformity were independent of inlet Mach number. However, the non-uniformity generally increased the off-incidence loss penalty. At low incidence, coating parameters of $k \leq 0.50$, resulted in loss and deviation predictions that were essentially equivalent to the uniformly coated profile. At higher positive and negative incidences, a coating parameter of $k = 0.50$ began to increase losses and deviation.

(4) The formation of a leading edge separation bubble was dependent on the absolute value of incidence, the coating profile parameter (k) and inlet Mach number. Increasing any of these values increases the likelihood of a leading edge separation bubble. A correlation of the numerical results shows attached flow is maintained when incidence (i) in radians is maintained as follows:

$$-1.2\left[\left(\frac{r}{c}\right)^{0.5}-0.15(k)^{2}\right]\sqrt{1-Ma^{2}}<i<1.2\left[\left(\frac{r}{c}\right)^{0.5}-0.3(k)^{4}\right]\sqrt{1-Ma^{2}} \qquad (10)$$

The coating non-uniformity (k) should be maintained less than 0.25 to avoid an increase in separation. A coating non-uniformity above 0.5 begins to severely limit the range of attached flow incidence. This correlates to controlling the coating formulation and application such that the shoulder height is maintained less than 20% above the uniform height. In practice this means controlling the coating height—or even the initial manufacturing tolerance—to within just 0.2 mils, which is a very difficult task.

APPENDIX A. AIRFOIL DATA

Table 7. NACA 65 (12)10 Airfoil Coordinates. (From: Ref [36])

NACA 65 (12)10 Airfoil Coordinates			
Convex Surface		Concave Surface	
Station x	Ordinate y	Station x	Ordinate y
0	0	0	0
0.161	.971	0.839	-0.371
0.374	1.227	1.126	-0.387
0.817	1.679	1.683	-0.395
1.981	2.599	3.019	-0.367
4.399	4.035	5.601	-0.243
6.868	5.178	8.132	-0.09
9.361	6.147	10.639	0.057
14.388	7.734	15.612	0.342
19.477	8.958	20.553	0.594
24.523	9.915	25.477	0.825
29.611	10.64	30.389	1.024
34.706	11.153	35.294	1.207
39.804	11.479	40.196	1.373
44.904	11.598	45.096	1.542
50	11.488	50	1.748
55.087	11.139	54.913	2.001
60.161	10.574	59.839	2.278
65.214	9.801	64.786	2.559
70.245	8.86	69.755	2.804
75.256	7.808	74.744	2.932
80.242	6.607	79.758	2.945
85.204	5.272	84.796	2.804
90.154	3.835	89.846	2.369
95.096	2.237	94.904	1.555
100.068	0.134	99.932	-0.134
L.E. Radius = 0.666; Slope through L.E. = 0.505			

Table 8. Additional Circular Leading Edge Points.

Leading Edge Points	
0.5350	-0.3476
0.3724	-0.3144
0.2232	-0.2420
0.0964	-0.1350
0	0
-0.0576	0.1454
-0.0798	0.3002
-0.0652	0.4559
-0.0147	0.6040

THIS PAGE INTENTIONALLY LEFT BLANK

APPENDIX B. GRID GENERATION PARAMETERS

The following code was the input file (*cdnew.ing*) for the grid generation program GRAPE.

```
&GRID1
 JMAX=360,KMAX=61,JTEBOT=80,JTETOP=281,NTETYP=3,NAIRF=5,
 NOBSHP=7,JAIRF=59,NIBDST=7,DSI=0.00004,XLEFT=-.5,
 XRIGHT=2.5,XLE=0.0,XTE=1.0,ALAMF=-10.0,ALAMR=0.0,
 RCORN=.125,NOUT=4,NORDA=0,3,MAXITA=0,500
 &END
 &GRID2
 PITCH=1.0,AAAI=.3,BBBI=.3,DSOBI=0.02,NLE=48,NTE=24,
 DSLE=.0008,DSTE=.0016,XTFRAC=1.0,ROTANG=-28.5,DSRA=.485,
 WAKEP=1.0,OMEGR=.6,OMEGS=.6,OMEGP=.6,OMEGQ=.6,
 &END
 &GRID3
 AIRFX=
 1.0013400e+02,9.4904000e+01,
 8.9846000e+01,8.4796000e+01,7.9758000e+01,7.4744000e+01,
 6.9755000e+01,6.4786000e+01,5.9839000e+01,5.4913000e+01,
 5.0000000e+01,4.5096000e+01,4.0196000e+01,3.5294000e+01,
 3.0389000e+01,2.5477000e+01,2.0553000e+01,1.5612000e+01,
 1.0639000e+01,8.1320000e+00,5.6010000e+00,3.0190000e+00,
 1.6830000e+00,1.1260000e+00,8.3900000e-01,5.3498773e-01,
 3.7244607e-01,2.2315806e-01,9.6387260e-02,0.0000000e+00,
 -5.763111e-02,-7.976608e-02,-6.518424e-02,-1.468973e-02,
 1.6100000e-01,3.7400000e-01,8.1700000e-01,1.9810000e+00,
 4.3990000e+00,6.8680000e+00,9.3610000e+00,1.4388000e+01,
 1.9477000e+01,2.4523000e+01,2.9611000e+01,3.4706000e+01,
 3.9804000e+01,4.4904000e+01,5.0000000e+01,5.5087000e+01,
 6.0161000e+01,6.5214000e+01,7.0245000e+01,7.5256000e+01,
 8.0242000e+01,8.5204000e+01,9.0154000e+01,9.5096000e+01,
 1.0013400e+02
 AIRFY=
 -6.800000e-02,1.5550000e+00,
 2.3690000e+00,2.8040000e+00,2.9450000e+00,2.9320000e+00,
 2.8040000e+00,2.5590000e+00,2.2780000e+00,2.0010000e+00,
 1.7480000e+00,1.5420000e+00,1.3730000e+00,1.2070000e+00,
 1.0240000e+00,8.2500000e-01,5.9400000e-01,3.4200000e-01,
 5.7000000e-02,-9.000000e-02,-2.430000e-01,-3.670000e-01,
 -3.950000e-01,-3.870000e-01,-3.71000e-01,-3.4762853e-01,
 -3.144087e-01,-2.4204547e-01,-1.3502905e-01,0.00000e+00,
 1.4539354e-01,3.0021819e-01,4.5593588e-01,6.0395930e-01,
 9.7100000e-01,1.2270000e+00,1.6790000e+00,2.5990000e+00,
 4.0350000e+00,5.1780000e+00,6.1470000e+00,7.7340000e+00,
 8.9580000e+00,9.9150000e+00,1.0640000e+01,1.1153000e+01,
 1.1479000e+01,1.1598000e+01,1.1488000e+01,1.1139000e+01,
 1.0574000e+01,9.8010000e+00,8.8600000e+00,7.8080000e+00,
 6.6070000e+00,5.2720000e+00,3.8350000e+00,2.2370000e+00,
 -6.8000000e-02
 &END
```

Notes:

1. JTEBOT sets number of points in wake. JTETOP is JMAX+1-JTEBOT.

2. NIBDST set to 7 for hermite polynomial clustering.

3. DSI set small for tight grid spacing away from the inner boundary.

4. PITCH controls solidity and set to one.

5. NLE and DSLE set the number spacing of points around the leading edge. NTE and DSTE set the same parameters for the trailing edge.

6. ROTANG sets the stagger angle (λ) of the airfoil and was set to negative λ (-28.5).

7. AIRFX and AIRFY were varied to account for non-uniform coating profiles. These values were obtained from output variables, XBc and YBc, in the MATLAB code in Appendix D.

APPENDIX C. CFD SOLVER (RVCQ3D) PARAMETERS

The following code was the input file (*rvcq3d.inr*) for the CFD program RVCQ3D.

```
'65 SERIES BLADE w/ coating'
 &NL1 M=360,N=61,MTL=80,MIL=152 &end
 &NL2 NSTG=4,IVDT=1,IRS=1,EPI=.30,EPJ=.40,CFL=4.0,
      AVISC2=1.0, EPS=0.4, AVISC4=1.0 &END
 &NL3 IBCIN=1,IBCEX=1,ITMAX=12000,IRESTI=0,IRESTO=1,IRES=1,ICRNT=10,
      IXRM=0 &END
 &NL4 AMLE=.76,ALLE=46,BETE=20,PRAT=0.844,P0IN=1.0,T0IN=1.0,G=1.40,
      &END
 &NL5 ILT=5,JEDGE=31,RENR=6e5,PRNR=.70,TW=0.0,VISPWR=.666666,
      CMUTM=14.0,ITUR=5 &END
 &NL6 OMEGA=0.0,NBLADE=1,NMN=2 &end
 &NL7 TINTENS=0.06,TMUIN=.01 &end
-.8000 4.500
1.0000 1.000
1.0000 0.970
```

Notes:

1. Artificial viscosity was set to 0.8 for the 0.6 Mach cases and 1.0 to maintain a stable solution for the 0.76 Mach number cases.

2. PRAT is the ratio of exit static pressure to inlet static pressure. This value will remain constant throughout the simulation. Additionally, the inlet rotational velocity is held constant based on AMLE (inlet Mach number) and ALLE (inlet air angle). However, the final inlet Mach number and Air Inlet Angle will vary to maintain PRAT and rotational velocity constant.

THIS PAGE INTENTIONALLY LEFT BLANK

APPENDIX D. AIRFOIL AND COATING CODE (MATLAB)

MATLAB Code used to fair circular leading edge points; calculate the coating thickness and normal direction from the baseline airfoil; add the coating height distribution to the baseline; verify conservation of coating for each profile; plot results; and output X-Y data vectors of grid points for the grid generation program GRAPE.

```
clear all
ler=.666;         % Leading edge radius
lep=9; lep_2=(lep+1)/2; % number of points on leading edge circle (must be odd)
%===========================================================================
% xs=suction side x coordinates; ys=suction side y coordinates
% xp=pressure side x coordinates; yp=pressure side y coordinates
xs=[0,0.161,0.374,0.817,1.981,4.399,6.868,9.361,14.388,19.477,24.523,29.611,
  34.706,39.804,44.904,50,55.087,60.161,65.214,70.245,75.256,80.242,85.204,
  90.154,95.096,100.068,];
xp=[0.839,1.126,1.683,3.019,5.601,8.132,10.639,15.612,20.553,25.477,30.389,35.2
  94,40.196,45.096,50,54.913,59.839,64.786,69.755,74.744,79.758,84.796,89.846,
  94.904,99.932,];
ys=[0,0.971,1.227,1.679,2.599,4.035,5.178,6.147,7.734,8.958,9.915,10.64,11.153,
  11.479,11.598,11.488,11.139,10.574,9.801,8.86,7.808,6.607,5.272,3.835,2.237,
  0.134];
yp=[-0.371,-0.387,-0.395,-0.367,-0.243,-0.09,0.057,0.342,0.594,0.825,1.024,
  1.207,1.373,1.542,1.748,2.001,2.278,2.559,2.804,2.932,2.945,2.804,2.369,1.555,
  -0.134];

% Assemble vectors of x and y coordinates from TE along PS thru LE & along SS
XX=[fliplr(xp) xs];
YY=[fliplr(yp) ys];

%========================================================================
% Define Leading edge circle
alpha=.5*(atan(YY(27)/XX(27))+atan(YY(25)/XX(25)));
xc=ler*cos(alpha); yc=ler*sin(alpha);

% Distance from center of LE circle to first blade points
d1=((XX(25)-xc)^2+(YY(25)-yc)^2)^.5;
d2=((XX(27)-xc)^2+(YY(27)-yc)^2)^.5;

% Angle of first blade points
phi1=atan((XX(25)-xc)/(yc-YY(25)));
phi2=atan((XX(27)-xc)/(yc-YY(27)));

% Angle between radial line to tangent point and line to 1st point
th1=acos(ler/d1);
th2=acos(ler/d2);

% LE circle angle to tangency point
psi1=3*pi/2+phi1-th1;
psi2=pi/2+phi2+th2;

% Define points on LE circle
t1=linspace(psi1,pi+alpha,lep_2);
t2=linspace(pi+alpha,psi2,lep_2);
t(1:lep_2)=t1; t(lep_2:lep)=t2;
xp=xc+ler*cos(t);
yp=yc+ler*sin(t);
```

```
% Insert LE circle points into blade XY coordinates
XB(3:27)=XX(1:25); XB(28:27+lep)=xp; XB(28+lep:52+lep)=XX(27:51);
YB(3:27)=YY(1:25); YB(28:27+lep)=yp; YB(28+lep:52+lep)=YY(27:51);

% Fair Trailing Edge Coordinates
TEA=atan((YB(61)-YB(3))/(XB(61)-XB(3)));
TER=sqrt((YB(61)-YB(3))^2+(XB(61)-XB(3))^2)/2;
XB(1)=.5*(XB(3)+XB(61))+cos(TEA-pi/2)*TER; XB(63)=XB(1);
YB(1)=.5*(YB(3)+YB(61))+sin(TEA-pi/2)*TER; YB(63)=YB(1);
XB(2)=.5*(XB(3)+XB(61))+cos(TEA-3*pi/4)*TER;
YB(2)=.5*(YB(3)+YB(61))+sin(TEA-3*pi/4)*TER;
XB(62)=.5*(XB(3)+XB(61))+cos(TEA-pi/4)*TER;
YB(62)=.5*(YB(3)+YB(61))+sin(TEA-pi/4)*TER;

% Assemble output matrix
XY=[XB;YB];

% Plot Baseline airfoil
figure(1); subplot(3,2,1)
plot(XB,YB,'b'); axis equal;hold on
axis([-1 7 -1 4])

%Calculate normal directions
for mc=3:length(XB)-2
    m(mc)=atan2(YB(mc+1)-YB(mc-1),XB(mc+1)-XB(mc-1));
end
n=m+pi/2;
n(1)=TEA-pi/2; n(63)=TEA-pi/2;
n(2)=TEA-3*pi/4; n(62)=TEA-pi/4;

% Calculate d_theta at airfoil points
for th=2:62
    d(th)=(n(th+1)-n(th-1))/2;
end
d(1)=.5*(n(2)-n(1)); d(63)=d(1);
d=abs(d);

%===============================
% Build Coating vs s
%===============================
kk=0; h0=0.18;  % Coating thickness

for k=.01:.25:1.01
    kk=kk+1;
    s(1)=0; s2(1)=0;

    % Calculate path length to each point along baseline airfoil
    for cs=1:31
    s(cs+1) = s(cs) + sqrt((XY(1,cs+30)-XY(1,cs+29))^2+(XY(2,cs+30)-
       XY(2,cs+29))^2);
    end
    ss=1.5*s;

    % Coating Family Curve Definition
    h=h0-(k/2)*exp(-.5*ss/(k/2)^1.1).* (ss.^1.4+.8*(k/2)^1.2).*
      cos(.56*ss/(k/2)^1.4);

    t=[fliplr(h) h(2:end)];  % Vector of local coating thickness

    XBc=XB+t.*cos(n); YBc=YB+t.*sin(n);

    % Calculate path length to each point along coated surface
    for cs2=1:31
```

```
        s2(cs2+1) = s2(cs2) + sqrt((XBc(cs2+30)-
          XBc(cs2+29))^2+(YBc(cs2+30)YBc(cs2+29))^2);
    end
    s_mid=.5*(s+s2);
    C(kk)=trapz(s_mid(1:10),h(1:10));

    % Calculate normal directions on coating surface
    for mc2=3:length(XBc)-2
        m2(mc2)=atan2(YBc(mc2+1)-YBc(mc2-1),XBc(mc2+1)-XBc(mc2-1));
    end
    n2=m2+pi/2;
    n2(1)=TEA-pi/2; n2(63)=TEA-pi/2;
    n2(2)=TEA-3*pi/4; n2(62)=TEA-pi/4;

    for rc=2:13
        radc(rc)=.5*(s2(rc)-s2(rc-1))/tan((n2(30+rc)-n2(31+rc))/2);
    end
    radc(1)=ler+h(1);

    figure(1); subplot(3,2,kk+1)
    plot(XB,YB,'k',XBc,YBc,'b'); axis equal;hold on
    axis([-1 7 -1 4])

    figure(2); plot(s,h,'g.-'); grid on; hold on
    axis([0 3 0 .5])

    figure(3); semilogy(s2(1:13),radc); hold on; grid on
    pause
end
Err2=100*(C-C(1))/C(1);
```

THIS PAGE INTENTIONALLY LEFT BLANK

APPENDIX E. DATA SUMMARY TABLES

Table 9. Numerical Simulation Results: Mach number effect.

Input		Output Values				Derived Values		Separation		Transition		Turb Sep
PR	k	A1	P1	PT2	Ma1	Loss	Turning	Suction	Pressure	Suction	Pressure	Suction
0.881	unc	45.0	0.7837	0.9952	0.60	2.210	23.456			19.1	19.2	93.0
0.881	0.00	45.1	0.7844	0.9951	0.60	2.255	23.156			19.1	19.2	93.0
0.881	0.25	45.1	0.7845	0.9951	0.60	2.260	23.151			19.1	19.2	93.0
0.881	0.50	45.1	0.7845	0.9951	0.60	2.265	23.146			19.1	19.2	93.0
0.881	0.75	45.1	0.7846	0.9951	0.60	2.279	23.131		2.4~3.2	19.1	19.2	93.0
0.881	1.00	45.2	0.7852	0.9949	0.60	2.389	23.036		3.0~4.7	18.4	4.4	92.0
0.868	unc	45.1	0.7532	0.9944	0.65	2.274	23.464			17.5	17.7	93.2
0.868	0.00	45.2	0.7542	0.9943	0.65	2.323	23.164			17.5	17.7	92.3
0.868	0.25	45.2	0.7542	0.9943	0.65	2.323	23.162			17.5	17.7	92.3
0.868	0.50	45.2	0.7542	0.9943	0.65	2.332	23.155			17.5	17.7	92.3
0.868	0.75	45.2	0.7543	0.9943	0.65	2.344	23.144		2.4~3.2	17.5	17.7	92.3
0.868	1.00	45.3	0.7549	0.0994	0.65	2.441	23.061	0.6~1.3	3.0~4.7	17.5	4.6	92.3
0.854	unc	45.0	0.7207	0.9933	0.70	2.385	23.209			16.1	14.2	92.3
0.854	0.00	45.1	0.7218	0.9932	0.70	2.437	22.911			15.9	16.3	92.3
0.854	0.25	45.1	0.7218	0.9932	0.70	2.441	22.909			15.9	16.3	92.3
0.854	0.50	45.1	0.7218	0.9932	0.70	2.449	22.902			16.0	16.3	92.3
0.854	0.75	45.1	0.7216	0.9933	0.70	2.411	22.922		2.4~3.4	16.0	16.3	92.3
0.854	1.00	45.2	0.7225	0.9930	0.70	2.527	22.834	0.6~1.3	2.9~4.8	16.0	4.2	91.3
0.840	unc	45.1	0.6828	0.9917	0.76	2.602	23.002			17.0	16.3	90.0
0.840	0.00	45.2	0.6842	0.9915	0.76	2.673	22.705			17.0	16.3	89.0
0.840	0.25	45.2	0.6842	0.9915	0.76	2.673	22.703			17.0	16.3	89.0
0.840	0.50	45.2	0.6843	0.9915	0.76	2.683	22.696			17.0	16.3	88.0
0.840	0.75	45.3	0.6845	0.9914	0.76	2.704	22.685		2.4~3.5	17.0	16.3	88.0
0.840	1.00	45.4	0.6854	0.9912	0.75	2.785	22.606	0.6~1.2	2.8~4.8	17.0	3.7	86.0
0.826	unc	45.0	0.6559	0.9884	0.80	3.345	22.468			20.7	13.6	86.7
0.826	0.00	45.1	0.6575	0.9882	0.80	3.425	22.179			20.6	14.9	85.3
0.826	0.25	45.1	0.6575	0.9882	0.80	3.425	22.177			20.6	14.9	85.3
0.826	0.50	45.2	0.6576	0.9882	0.80	3.435	22.170			20.6	14.9	85.3
0.826	0.75	45.2	0.6578	0.9881	0.80	3.458	22.164		2.3~3.8	20.6	16.4	83.9
0.826	1.00	45.3	0.6587	0.9879	0.80	3.519	22.074	.7~1.1	2.8~5.2	20.6	3.6	83.9

Key:

PR is static pressure ratio (PRAT), **k** is the coating non-uniformity parameter, **A1** is the inlet air angle (α_1), **P1** is the inlet static pressure, **PT2** is the exit stagnation pressure, **Ma1** is the inlet Mach number, and **Loss** is the total pressure loss coefficient $(\bar{\varpi})$. **Separation** shows regions of separation (in % chord) on the suction or pressure side based on skin friction. **Transition** shows the approximate beginning of the transition region (in % chord) based on growth of turbulent viscosity on the surface. **Turb Sep** shows where the turbulent boundary layer separated from the suction surface based on skin friction.

Table 10. Numerical Simulation Results: Ma = 0.6, Negative Incidence.

Input		Output Values				Derived Values		Separation		Transition		Turb Sep
PR	k	A1	P1	PT2	Ma1	Loss	Turning	Suction	Pressure	Suction	Pressure	Suction
0.856	unc	39.3	0.7866	0.9948	0.60	2.451	18.250		1.3~4.5	20.7	3.9	95.0
0.856	0.00	39.4	0.7874	0.9947	0.59	2.508	17.965		1.6~4.6	20.7	4.1	94.0
0.856	0.25	39.4	0.7875	0.9947	0.59	2.513	17.961		1.6~4.5	20.7	4.0	94.0
0.856	0.50	39.4	0.7877	0.9946	0.59	2.553	17.940		1.6~3.1	20.7	2.7	94.0
0.856	0.75	39.5	0.7878	0.9945	0.59	2.568	17.931		2.2~4.0	20.7	2.7	94.0
0.856	1.00	39.5	0.7882	0.9944	0.59	2.658	17.905		2.6~6.0	20.7	3.3	94.0
0.861	unc	40.3	0.7863	0.9950	0.60	2.321	19.263		1.4~3.9	20.7	14.9	95.0
0.861	0.00	40.4	0.7871	0.9950	0.59	2.367	18.971		1.7~4.8	20.7	14.9	94.0
0.861	0.25	40.4	0.7871	0.9949	0.59	2.373	18.968		1.7~5.3	20.7	14.9	94.0
0.861	0.50	40.4	0.7874	0.9948	0.59	2.423	18.934		1.7~6.3	20.7	6.8	94.0
0.861	0.75	40.4	0.7876	0.9948	0.59	2.463	18.912		2.2~3.6	20.7	2.8	94.0
0.861	1.00	40.5	0.7879	0.9947	0.59	2.518	18.886		2.5~5.5	20.7	3.5	93.0
0.865	unc	41.2	0.7855	0.9951	0.60	2.271	20.130			20.7	16.3	95.0
0.865	0.00	41.3	0.7863	0.9950	0.60	2.317	19.836			20.7	17.7	94.0
0.865	0.25	41.3	0.7864	0.9950	0.60	2.317	19.834			20.7	16.3	94.0
0.865	0.50	41.3	0.7864	0.9950	0.60	2.327	19.823		1.7~2.6	20.7	16.3	94.0
0.865	0.75	41.3	0.7865	0.9950	0.60	2.332	19.813		2.2~5.2	20.7	15.0	94.0
0.865	1.00	41.4	0.7870	0.9948	0.60	2.427	19.757		2.7~5.4	20.7	3.5	94.0
0.869	unc	42.1	0.7851	0.9951	0.60	2.261	20.964			19.1	17.7	95.0
0.869	0.00	42.2	0.7857	0.9951	0.60	2.277	20.687			19.0	17.7	94.0
0.869	0.25	42.2	0.7857	0.9951	0.60	2.282	20.685			19.0	17.7	94.0
0.869	0.50	42.2	0.7857	0.9951	0.60	2.287	20.679		1.6~2.2	19.0	17.7	94.0
0.869	0.75	42.2	0.7857	0.9951	0.60	2.283	20.672		2.2~4.1	19.0	17.7	94.0
0.869	1.00	42.3	0.7863	0.9949	0.60	2.392	20.596		2.8~5.2	19.0	3.3	94.0
0.873	unc	43.1	0.7845	0.9952	0.60	2.232	21.804			17.5	17.7	94.0
0.873	0.00	43.2	0.7851	0.9952	0.60	2.248	21.528			19.0	17.7	94.0
0.873	0.25	43.2	0.7853	0.9951	0.60	2.282	21.506			19.0	17.7	94.0
0.873	0.50	43.2	0.7852	0.9951	0.60	2.253	21.522		1.8~2.0	19.0	17.7	94.0
0.873	0.75	43.2	0.7852	0.9951	0.60	2.253	21.517		2.3~3.7	19.1	19.8	94.0
0.873	1.00	43.2	0.7857	0.9950	0.60	2.347	21.441		2.8~4.9	19.1	3.7	94.0
0.877	unc	44.0	0.7841	0.9952	0.60	2.218	22.636			19.1	19.3	93.0
0.877	0.00	44.1	0.7848	0.9951	0.60	2.268	22.334			19.0	19.2	93.0
0.877	0.25	44.1	0.7849	0.9951	0.60	2.268	22.332			19.0	19.2	93.0
0.877	0.50	44.1	0.7849	0.9951	0.60	2.273	22.327			19.6	20.9	93.0
0.877	0.75	44.1	0.7847	0.9952	0.60	2.234	22.347		2.2~3.4	20.7	4.1	93.0
0.877	1.00	44.2	0.7852	0.9950	0.60	2.318	22.275	0.7~1.0	3.0~4.5	20.7	4.1	93.0

Key:

PR is static pressure ratio (PRAT), **k** is the coating non-uniformity parameter, **A1** is the inlet air angle (α_1), **P1** is the inlet static pressure, **PT2** is the exit stagnation pressure, **Ma1** is the inlet Mach number, and **Loss** is the total pressure loss coefficient $(\bar{\omega})$. **Separation** shows regions of separation (in % chord) on the suction or pressure side based on skin friction. **Transition** shows the approximate beginning of the transition region (in % chord) based on growth of turbulent viscosity on the surface. **Turb Sep** shows where the turbulent boundary layer separated from the suction surface based on skin friction.

Table 11. Numerical Simulation Results: Ma = 0.6, Zero and Positive Incidence.

Input		Output Values				Derived Values		Separation		Transition		Turb Sep
PR	k	A1	P1	PT2	Ma1	W	Turning	Suction	Pressure	Suction	Pressure	Suction
0.881	unc	45.0	0.7837	0.9952	0.60	2.210	23.456			19.1	19.2	93.0
0.881	0.00	45.1	0.7844	0.9951	0.60	2.255	23.156			19.1	19.2	93.0
0.881	0.25	45.1	0.7845	0.9951	0.60	2.260	23.151			19.1	19.2	93.0
0.881	0.50	45.1	0.7845	0.9951	0.60	2.265	23.146			19.1	19.2	93.0
0.881	0.75	45.1	0.7846	0.9951	0.60	2.279	23.131		2.4~3.2	19.1	19.2	93.0
0.881	1.00	45.2	0.7852	0.9949	0.60	2.389	23.036		3.0~4.7	18.4	4.4	92.0
0.886	unc	46.1	0.7844	0.9952	0.60	2.217	24.385			17.5	19.3	93.0
0.886	0.00	46.2	0.7851	0.9951	0.60	2.267	24.078			17.5	19.3	92.0
0.886	0.25	46.2	0.7851	0.9951	0.60	2.271	24.076			17.5	19.2	92.0
0.886	0.50	46.2	0.7852	0.9951	0.60	2.272	24.070			17.5	19.2	92.0
0.886	0.75	46.2	0.7850	0.9952	0.60	2.242	24.088	0.2~0.5	2.4~3.0	19.1	20.9	92.0
0.886	1.00	46.2	0.7853	0.9950	0.60	2.301	24.034	0.5~1.5	3.1~5.0	19.1	20.9	92.0
0.890	unc	47.1	0.7845	0.9951	0.60	2.283	25.149			17.5	20.8	92.0
0.890	0.00	47.2	0.7850	0.9951	0.60	2.293	24.873			17.5	20.8	92.0
0.890	0.25	47.2	0.7850	0.9951	0.60	2.293	24.870			17.5	20.8	91.0
0.890	0.50	47.2	0.7851	0.9950	0.60	2.303	24.863			17.5	20.8	91.0
0.890	0.75	47.2	0.7850	0.9951	0.60	2.284	24.874	0.2~0.6	2.5~2.7	17.5	20.8	91.0
0.890	1.00	47.2	0.7850	0.9951	0.60	2.293	24.873			17.4	20.8	91.0
0.894	unc	48.1	0.7846	0.9950	0.60	2.335	25.925			16.0	22.5	90.0
0.894	0.00	48.2	0.7853	0.9949	0.60	2.390	25.613			15.9	22.5	90.0
0.894	0.25	48.2	0.7854	0.9948	0.60	2.400	25.609			17.5	22.5	90.0
0.894	0.50	48.2	0.7852	0.9949	0.60	2.355	25.636			17.5	22.5	90.0
0.894	0.75	48.2	0.7854	0.9948	0.60	2.410	25.597	0.2~0.7		17.5	24.2	90.0
0.894	1.00	48.4	0.7865	0.9944	0.60	2.618	25.454	0.3~2.1	3.5~4.2	16.1	24.2	88.0
0.898	unc	49.2	0.7850	0.9948	0.60	2.423	26.673			16.0	22.4	86.0
0.898	0.00	49.3	0.7857	0.9947	0.60	2.487	26.357			15.9	22.4	84.0
0.898	0.25	49.3	0.7857	0.9946	0.60	2.497	26.350			15.9	22.4	84.0
0.898	0.50	49.3	0.7858	0.9946	0.60	2.517	26.335			16.1	22.5	85.0
0.898	0.75	49.4	0.7864	0.9944	0.60	2.631	26.264	0.2~0.8		16.1	24.2	84.0
0.898	1.00	49.8	0.7886	0.9935	0.59	3.074	26.008	0.3~2.3		11.9	26.0	80.0
0.902	unc	50.4	0.7861	0.9943	0.60	2.660	27.329			14.5	26.0	80.0
0.902	0.00	50.5	0.7868	0.9942	0.60	2.730	27.010			14.5	25.9	79.0
0.902	0.25	50.5	0.7869	0.9941	0.60	2.750	26.998			14.5	25.9	79.0
0.902	0.50	50.5	0.7871	0.9941	0.60	2.785	26.976	0.1~.016		14.5	24.2	79.0
0.902	0.75	50.8	0.7887	0.9934	0.59	3.124	26.798	0.2~9.6		12.0	26.0	77.0
0.902	1.00	50.5	0.8139	0.9816	0.55	4.881	26.188	0.2~2.2		0.5	29.0	34.0

Key:

PR is static pressure ratio (PRAT), **k** is the coating non-uniformity parameter, **A1** is the inlet air angle (α_1), **P1** is the inlet static pressure, **PT2** is the exit stagnation pressure, **Ma1** is the inlet Mach number, and **Loss** is the total pressure loss coefficient $(\bar{\varpi})$. **Separation** shows regions of separation (in % chord) on the suction or pressure side based on skin friction. **Transition** shows the approximate beginning of the transition region (in % chord) based on growth of turbulent viscosity on the surface. **Turb Sep** shows where the turbulent boundary layer separated from the suction surface based on skin friction.

Table 12. Numerical Simulation Results: Ma = 0.75, Negative Incidence.

Input		Output Values				Derived Values		Separation		Transition		Turb Sep
PR	k	A1	P1	PT2	Ma1	W	Turning	Suction	Pressure	Suction	Pressure	Suction
0.814	unc	40.4	0.6978	0.9917	0.74	2.754	18.818		1.4~4.4	22.0	3.3	93.0
0.814	0.00	40.5	0.6992	0.9915	0.73	2.823	18.549		1.6~4.4	22.0	3.4	93.0
0.814	0.25	40.5	0.6993	0.9915	0.73	2.830	18.546		1.6~4.4	22.0	3.3	93.0
0.814	0.50	40.6	0.6997	0.9913	0.73	2.885	18.527		1.7~4.2	22.0	2.6	93.0
0.814	0.75	40.6	0.6999	0.9913	0.73	2.906	18.519		2.2~4.3	22.0	2.7	93.0
0.814	1.00	40.7	0.7011	0.9908	0.73	3.062	18.474		2.6~6.5	21.0	3.3	93.0
0.816	unc	41.0	0.6927	0.9917	0.74	2.698	19.354		1.4~5.2	20.7	4.8	93.0
0.816	0.00	41.1	0.6942	0.9915	0.74	2.770	19.079		1.7~5.0	20.7	4.4	93.0
0.816	0.25	41.1	0.6943	0.9915	0.74	2.777	19.076		1.6~5.0	20.7	4.4	93.0
0.816	0.50	41.1	0.6946	0.9914	0.74	2.817	19.051		1.7~5.0	20.7	3.6	93.0
0.816	0.75	41.2	0.6949	0.9913	0.74	2.845	19.042		2.2~4.1	20.7	2.7	93.0
0.816	1.00	41.2	0.6957	0.9910	0.74	2.951	19.016		2.6~6.1	20.7	3.3	93.0
0.820	unc	41.6	0.6890	0.9920	0.75	2.579	20.076		1.5~5.7	20.7	13.6	93.0
0.820	0.00	41.8	0.6904	0.9918	0.75	2.639	19.793		1.7~8.4	19.3	13.6	92.0
0.820	0.25	41.8	0.6904	0.9918	0.75	2.646	19.789		1.7~8.4	19.3	13.6	92.0
0.820	0.50	41.8	0.6909	0.9916	0.75	2.702	19.756		1.7~5.6	19.0	4.9	92.0
0.820	0.75	41.9	0.6913	0.9915	0.75	2.741	19.738		2.2~3.9	19.1	2.8	92.0
0.820	1.00	42.0	0.6923	0.9912	0.74	2.857	19.684		2.7~5.8	19.1	3.3	92.0
0.826	unc	42.5	0.6876	0.9922	0.75	2.497	20.936			19.1	14.9	93.0
0.826	0.00	42.7	0.6890	0.9920	0.75	2.556	20.650			19.0	14.9	92.0
0.826	0.25	42.7	0.6890	0.9920	0.75	2.560	20.648			19.0	14.9	92.0
0.826	0.50	42.7	0.6892	0.9920	0.75	2.574	20.634		1.7~2.7	19.0	14.8	92.0
0.826	0.75	42.7	0.6892	0.9920	0.75	2.581	20.622		2.2~7.5	19.0	13.7	92.0
0.826	1.00	42.8	0.6906	0.9915	0.75	2.732	20.539		2.7~5.5	18.7	3.5	91.0
0.832	unc	43.5	0.6871	0.9921	0.75	2.506	21.752			17.5	14.9	92.0
0.832	0.00	43.6	0.6884	0.9920	0.75	2.565	21.462			17.5	14.9	92.0
0.832	0.25	43.6	0.6884	0.9920	0.75	2.568	21.461			17.5	14.9	91.0
0.832	0.50	43.6	0.6885	0.9919	0.75	2.578	21.452		1.8~2.2	17.3	14.9	91.0
0.832	0.75	43.7	0.6886	0.9919	0.75	2.586	21.442		2.3~4.1	17.2	15.0	91.0
0.832	1.00	43.7	0.6894	0.9917	0.75	2.663	21.383		2.7~5.5	17.5	3.5	91.0
0.836	unc	44.3	0.6847	0.9920	0.76	2.528	22.389			17.5	16.3	91.0
0.836	0.00	44.4	0.6861	0.9918	0.75	2.590	22.096			17.4	16.3	90.0
0.836	0.25	44.4	0.6861	0.9918	0.75	2.594	22.095			17.4	16.3	90.0
0.836	0.50	44.4	0.6862	0.9918	0.75	2.601	22.087		1.8~2.2	17.4	16.3	90.0
0.836	0.75	44.4	0.6863	0.9918	0.75	2.615	22.077		2.3~4.1	17.4	16.3	90.0
0.836	1.00	44.5	0.6873	0.9915	0.75	2.712	21.998	0.6~1.0	2.7~5.2	17.4	3.6	89.0

Key:

PR is static pressure ratio (PRAT), **k** is the coating non-uniformity parameter, **A1** is the inlet air angle (α_1), **P1** is the inlet static pressure, **PT2** is the exit stagnation pressure, **Ma1** is the inlet Mach number, and **Loss** is the total pressure loss coefficient $(\bar{\omega})$. **Separation** shows regions of separation (in % chord) on the suction or pressure side based on skin friction. **Transition** shows the approximate beginning of the transition region (in % chord) based on growth of turbulent viscosity on the surface. **Turb Sep** shows where the turbulent boundary layer separated from the suction surface based on skin friction.

Table 13. Numerical Simulation Results: Ma = 0.75, Zero and Positive Incidence.

Input		Output Values				Derived Values		Separation		Transition		Turb Sep
PR	k	A1	P1	PT2	Ma1	W	Turning	Suction	Pressure	Suction	Pressure	Suction
0.840	unc	45.1	0.6828	0.9917	0.76	2.602	23.002			17.0	16.3	90.0
0.840	0.00	45.2	0.6842	0.9915	0.76	2.673	22.705			17.0	16.3	89.0
0.840	0.25	45.2	0.6842	0.9915	0.76	2.673	22.703			17.0	16.3	89.0
0.840	0.50	45.2	0.6843	0.9915	0.76	2.683	22.696			17.0	16.3	88.0
0.840	0.75	45.3	0.6845	0.9914	0.76	2.704	22.685		2.4~3.5	17.0	16.3	88.0
0.840	1.00	45.4	0.6854	0.9912	0.75	2.785	22.606	0.6~1.2	2.8~4.8	17.0	3.7	86.0
0.844	unc	46.0	0.6820	0.9908	0.76	2.796	23.561			16.0	16.3	86.0
0.844	0.00	46.2	0.6835	0.9908	0.76	2.879	23.258			15.9	16.3	84.0
0.844	0.25	46.2	0.6835	0.9908	0.76	2.882	23.257			15.9	16.3	84.0
0.844	0.50	46.2	0.6836	0.9908	0.76	2.896	23.248			15.9	16.3	84.0
0.844	0.75	46.2	0.6838	0.9903	0.76	2.910	23.240	0.3~0.4	2.4~3.2	15.9	16.3	84.0
0.844	1.00	46.3	0.6851	0.9902	0.76	3.059	23.145	0.5~1.5	2.9~4.8	15.5	3.8	82.0
0.848	unc	47.0	0.6817	0.9902	0.76	3.051	24.116			15.0	16.3	82.0
0.848	0.00	47.1	0.6832	0.9900	0.76	3.148	23.810			14.8	16.3	81.0
0.848	0.25	47.1	0.6833	0.9900	0.76	3.151	23.809			14.8	16.3	81.0
0.848	0.50	47.2	0.6835	0.9899	0.76	3.179	23.798			14.6	16.3	81.0
0.848	0.75	47.2	0.6834	0.9899	0.76	3.163	23.791	0.2~0.5	2.4~3.0	14.6	17.0	79.0
0.848	1.00	47.4	0.6856	0.9892	0.75	3.426	23.697	0.5~1.5	3.1~5.2	14.5	17.0	79.0
0.853	unc	48.3	0.6846	0.9887	0.76	3.574	24.705			13.2	16.3	76.0
0.853	0.00	48.5	0.6862	0.9883	0.75	3.691	24.391			13.1	16.3	74.0
0.853	0.25	48.5	0.6863	0.9883	0.75	3.702	24.389			13.1	16.3	74.0
0.853	0.50	48.5	0.6867	0.9882	0.75	3.744	24.377			13.1	16.3	74.0
0.853	0.75	48.6	0.6867	0.9882	0.75	3.749	24.360	0.2~0.7	2.6~2.7	13.1	16.3	74.0
0.853	1.00	48.8	0.6889	0.9875	0.75	4.002	24.290	0.5~1.9	3.3~4.5	12.9	17.0	70.0
0.855	unc	49.4	0.6853	0.9864	0.75	4.288	24.989			11.9	16.3	68.0
0.855	0.00	49.6	0.6871	0.9861	0.75	4.424	24.670			11.9	16.3	66.0
0.855	0.25	49.6	0.6872	0.9860	0.75	4.439	24.668			11.9	16.3	66.0
0.855	0.50	49.7	0.6874	0.9860	0.75	4.454	24.658			11.9	16.3	66.0
0.855	0.75	49.8	0.6886	0.9856	0.75	4.609	24.633	0.2~0.7		11.9	16.3	66.0
0.855	1.00	49.6	0.6871	0.9863	0.75	4.367	24.603	0.7~1.9	3.4~4.1	11.8	16.3	66.0
0.856	unc	51.0	0.6899	0.9827	0.75	5.539	25.351	11~15		10.6	17.7	60.0
0.856	0.00	51.5	0.6933	0.9817	0.74	5.929	25.048	11~15		10.5	17.7	58.0
0.856	0.25	51.5	0.6936	0.9816	0.74	5.978	25.051	11~15		10.4	17.7	58.0
0.856	0.50	51.5	0.6936	0.9816	0.74	5.978	25.042	11~15		10.3	17.7	56.0
0.856	0.75	51.4	0.6931	0.9819	0.74	5.864	24.995	11~15		10.0	17.7	57.0
0.856	1.00	52.5	0.7007	0.9789	0.73	7.041	25.144	0.9~11.9		8.4	17.7	54.0

Key:

PR is static pressure ratio (PRAT), **k** is the coating non-uniformity parameter, **A1** is the inlet air angle (α_1), **P1** is the inlet static pressure, **PT2** is the exit stagnation pressure, **Ma1** is the inlet Mach number, and **Loss** is the total pressure loss coefficient $(\bar{\varpi})$. **Separation** shows regions of separation (in % chord) on the suction or pressure side based on skin friction. **Transition** shows the approximate beginning of the transition region (in % chord) based on growth of turbulent viscosity on the surface. **Turb Sep** shows where the turbulent boundary layer separated from the suction surface based on skin friction.

THIS PAGE INTENTIONALLY LEFT BLANK

LIST OF REFERENCES

1. Abbot, I. H. and Von Doenhoff, A. E., *Theory of Wing Sections*, Dover Publications, 1959, pp. 157-8.

2. Gostelow, J. P., *Cascade Aerodynamics*, Pergamon Press, 1984, pp. 238-241.

3. Schlichting, H., *Boundary Layer Theory*, 7th ed., McGraw-Hill, 1979, p. 659.

4. Caguiat, D. E., "Rolls Royce/Allison 501-K Gas Turbine Antifouling Compressor Coatings Evaluation," *Transactions of the ASME, Journal of Turbomachinery*, Volume 125, Number 3, July 2003, pp. 482-488.

5. Schwartz, L. W., 28 November 2003.

6. Schwartz, L. W. and Weidner, D. E., "Modeling of Coating Flows on Curved Surfaces," *Journal of Engineering Mathematics*, Volume 29, 1995, pp. 91-103.

7. Eley, R. R. and Schwartz L. W., "Interaction of Rheology, Geometry, and Process in Coating Flow," *Journal of Coatings Technology*, Volume 74, 2002, pp. 43-53.

8. Reid, L. and Urasek, D. C., "Experimental Evaluation of the Effects of a Blunt Leading Edge on the Performance of a Transonic Rotor," *Transactions of the ASME, Journal of Engineering for Power*, July 1973, pp. 199-204.

9. Roberts, W. B., "Axial Compressor Performance Restoration by Blade Profile Control," ASME Paper 84-GT-232, 1984.

10. Roberts, W. B., "Advanced Turbofan Blade Refurbishment Technique," *Transactions of the ASME, Journal of Turbomachinery* Technical Brief, Volume 117, October 1995, pp. 666-667.

11. Suder, K. L., Chima, R. V., Strazisar, A. J. and Roberts, W. B., "The Effect of Adding Roughness and Thickness to a Transonic Axial Compressor Rotor," *Transactions of the ASME, Journal of Turbomachinery,* Volume 117, Number 4, October 1995, pp 491-505.

12. Kwon, O. J. and Sankar, L. N., "Numerical Simulation of the Flow about a Swept Wing with Leading Edge Ice Accretions," *Computers and Fluids* Volume 26-2, 1997.

13. Khalid, M., Zhang, S. and Chen, S., "A Study of Aerodynamic Performance Degradation on Aerofoils and Aircraft Wings Due to Accreted Ice," *Aeronautical Journal*, Volume 106, September 2002.

14. Huebsch, W. W. and Rothmayer, A. P., "Effects of Ice Roughness on Dynamic Stall," *Journal of Aircraft*, Volume 39, Number 6, November-December 2002, pp 945-953.

15. Tuck, E. O., "A Criteria for Leading Edge Separation," *Journal of Fluid Mechanics*, Volume 222, 1991, pp 33-37.

16. Walraevens, R. E. and Cumpsty, N. A., "Leading-Edge Separation Bubbles on Turbomachine Blades," *Transactions of the ASME, Journal of Turbomachinery*, Volume 117, Number 1, January 1995.

17. Tain, L., *Compressor Leading Edges in Incompressible and Compressible Flows*, Doctoral Dissertation, Cambridge University, 1998.

18. Huoxing, L., Baojie, L., Ling, L., and Haokang, J., "Effect of Leading-Edge Geometry on Separation Bubble on a Compressor Blade," Proceedings of ASME Turbo Expo 2003, GT2003-38217.

19. Gostelow, J. P. and Walker, G. J., "Similarity Behavior in Transitional Boundary Layers over a Range of Adverse Pressure Gradients and Turbulence Levels," *Transactions of the ASME, Journal of Turbomachinery*, Volume 113, Number 4, October 1991, pp 617-625.

20. Gostelow, J. P., Blunden, A. R. and Walker, G. J., "Effects of Free-Stream Turbulence and Adverse Pressure Gradients on Boundary Layer Transition," *Transactions of the ASME, Journal of Turbomachinery*, Volume 116, Number 3, July 1994, pp 392-404.

21. Mayle, R. E., "The Role of Laminar-Turbulent Transition in Gas Turbine Engines," *Transactions of the ASME, Journal of Turbomachinery*, Volume 113, Number 4 October 1991, pp 509-537.

22. Walker, G. J., "The Role of Laminar Turbulent Transition in Gas Turbine Engines: A Discussion," *Transactions of the ASME, Journal of Turbomachinery*, Volume 115, Number 2, April 1993, pp 207-217.

23. Malkiel, E. and Mayle, R. E., "Transition in a Separation Bubble," *Transactions of the ASME, Journal of Turbomachinery*, Volume 118, Number 4, October 1996, pp 752-759.

24. Solomon, W. J., Walker, G. J., and Gostelow, J. P., "Transition Length Prediction for Flows with Rapidly Changing Pressure Gradients," *Transactions of the ASME, Journal of Turbomachinery*, Volume 118, Number 4, October 1996, pp 744-751.

25. Solomon, W. J., Walker, G. J., and Hughes, J. D., "Periodic Transition on an Axial Compressor Stator: Incidence and Clocking Effect: Part II – Transition Onset Predictions," *Transactions of the ASME, Journal of Turbomachinery*, Volume 121, Number 3, July 1999, pp 408-415.

26. Johnson, M. W., "Predicting Transition without Empiricism or DNS," *Transactions of the ASME, Journal of Turbomachinery*, Volume 124, Number 4,October 2002, pp 665-669.

27. Drela, M. and Giles, M. B., "Viscous-Inviscid Analysis of Transonic and Low Reynolds Number Airfoils," *AIAA Journal,* Volume 25, Number 10, October 1987, pp 1347-1355.

28. Sanz, W. and Platzer, M. F., "On the Navier-Stokes Calculation of Separation Bubbles with a New Transition Model," *Transactions of the ASME, Journal of Turbomachinery*, Volume 120, Number 1, January 1998, pp 36-42.

29. Tain L. and Cumpsty, N. A., "Compressor Blade Leading Edges in Subsonic Compressible Flow," *Proceedings of the Institution of Mechanical Engineers*, Volume 214, Part C, 2000, pp 221-242.

30. Hobson, G. V. and Weber, S., "Prediction of Laminar Separation Bubble over a Controlled Diffusion Compressor Blade,", Proceedings of ASME TurboExpo 2000, Munich, Germany, May 8-11, 2000, ASME Paper 2000-GT-277.

31. Wilcox, D. C., *Turbulence Modeling for CFD*, DCW Industries, 2nd Ed, 1998.

32. Steger, J. L., and Sorenson, R. L., "Automatic Mesh Point Clustering Near A Boundary in Grid Generation with Elliptic Partial Differential Equation," *Journal of Computational Physics*, Volume 33, Number 3, December 1979, pp. 405-410.

33. Sorenson, R. L., "A Computer Program to Generate Two-Dimensional Grids About Airfoils and Other Shapes by Use of Poisson's Equation," NASA TM-81198, 1980.

34. Chima, R. V., "GRAPE 2-D Grid Generator for Turbomachinery: User's Manual and Documentation," Version 104, 1997.

35. Chima, R. V., "Explicit Multigrid Algorithm for Quasi-Three-Dimensional Viscous Flows in Turbomachinery," *Journal of Propulsion and Power*, Volume 3, Number 5, September-October 1987, pp. 397-405.

36. Chima, R. V., Turkel, E., and Schaffer, S., "Comparison of Three Explicit Multigrid Methods for the Euler and Navier Stokes Equations," NASA TM-88878, January 1987.

37. Chima, R. V., "RVCQ3D – Rotor Viscous Code Quasi-3-D: User's Manual and Documentation," Version 303, 1999.

38. Felix, A. R. and Emery, J. C., "A Comparison of Typical National Gas Turbine Establishment and NACA Axial-Flow Compressor Blade Sections in Cascade at Low Speed," NACA TN 3937, March 1957.

39. Briggs, W. B., "Effect of Mach Number on the Flow and Application of Compressibility Corrections in a Two-Dimensional Subsonic-Transonic Compressor Cascade having Varied Porous Wall Suction at the Blade Tips," NACA TN 2649, March 1952.

40. Cumpsty, N. A., *Compressor Aerodynamics*, Longman Scientific and Technical, 1989, p. 162.

41. Lieblein, S., "Experimental Flow in Two-Dimensional Cascades," *Aerodynamic Design of Axial Flow Compressors: NASA SP-36*, Revised 1965, p. 190.

42. Menter, F. R., "Two-Equation Eddy-Viscosity Turbulence Models for Engineering Applications," *AIAA Journal*, Volume 32, August 1994, pp. 1598-1605.

43. Hill, P. G., and Peterson, R., Mechanics and Thermodynamics of Propulsion, 2nd Edition, Addison-Wesley Publishing, 1992.

INITIAL DISTRIBUTION LIST

1. Defense Technical Information Center
Fort Belvoir, Virginia

2. Dudley Knox Library
Naval Postgraduate School
Monterey, California

3. Professor Knox T. Millsaps
Department of Mechanical and Astronautical Engineering
Naval Postgraduate School
Monterey, California

4. Professor Garth V. Hobson
Department of Mechanical and Astronautical Engineering
Naval Post Graduate School
Monterey, California

5. Research Professor Muguru S. Chandrasekhara
Navy-NASA Joint Institute of Aerospace Sciences
NASA Ames Research Center
Moffett Field, California

6. Professor Leonard W. Schwartz
Department of Mechanical Engineering
University of Delaware
Newark, Delaware

7. Jeffrey S. Patterson
Gas Turbine Emerging Technologies Section
NSWC-Carderock Division
Philadelphia, Pennsylvania

8. Daniel E. Caguiat
Gas Turbine Emerging Technologies Section
NSWC-Carderock Division
Philadelphia, Pennsylvania

9. Nicholas A. Cumpsty
Chief Technologist
Rolls-Royce
Derby, England